Topographic metrics for unveiling fault segmentation and tectono-geomorphic evolution with insights into the impact of inherited topography, Ulsan Fault Zone, Korea

Cho-Hee Lee[1], Yeong Bae Seong[1], John Weber[2], Sangmin Ha[1], Dong-Eun Kim[3], Byung Yong Yu[4]

[1]Department of Geography, Korea University, Seoul, 02841, Republic of Korea
[2]Department of Geology, Grand Valley State University, Allendale, Michigan, 49401, USA
[3]Active Tectonics Research Center, Korea Institute of Geoscience and Mineral Resources, Daejeon, 34132, Republic of Korea
[4]Laboratory of Accelerator Mass Spectrometry, Korea Institute of Science and Technology, Seoul, 02792, Republic of Korea

Correspondence to: Yeong Bae Seong (ybseong@korea.ac.kr)

Abstract. Quantifying ~~the present~~ today's topography can provide insights into landscape evolution and its controls, since ~~the~~ present topography represents a cumulative expression of past and present surface processes. The Ulsan Fault Zone (UFZ) is an active fault zone on the southeastern Korean Peninsula, that was reactivated as a reverse fault around 5 Ma. ~~This NNW–SSE-trending fault zone exhibits a predominantly reverse sense of movement today, dipping~~ The UFZ strikes NNW–SSE and dips ~~towards the~~ eastward. This study investigates ~~the~~ relative tectonic activity along the UFZ and ~~the~~ landscape evolution of the hanging wall side of the UFZ, focusing on neotectonic perturbations using ^{10}Be-derived catchment-averaged denudation rates and bedrock incision rates, topographic metrics, and a landscape evolution model. ~~We evaluated the spatial variation in the relative tectonic activity from the variation in topographic metrics along the UFZ.~~ Five geological segments were identified along the fault, based on ~~the~~ their relative tectonic activity and fault geometry. We ~~then~~ simulated four cases of landscape evolution to investigate the geomorphic processes and accompanying topographic changes in the study area in response to fault movement~~s~~. ~~The m~~Model results reveal that the geomorphic processes and the patterns of topographic metrics (e.g., χ anomalies) depend on ~~the~~ inherited topography (i.e., the topography that existed prior to reverse fault~~ing~~ reactivation ~~on~~of the UFZ). On the basis of this important model finding and additional topographic metrics, we interpret the tectono-geomorphic history of the study area as follows: (1) the northern part of the UFZ has been in a transient state and is in topographic and geometric disequilibrium~~,~~; ~~as~~ this part underwent asymmetric uplift (westward tilting) prior to reverse faulting on the UFZ around 5 Ma; and (2) its southern part was negligibly influenced by the asymmetric uplift before reverse faulting. Our study demonstrates the utility of topographic metrics as reliable criteria for resolving ~~segmenting~~ fault~~s~~ segments. ~~Alongside~~ Together with landscape evolution modelling, ~~these~~ topographic metrics ~~are instrumental in~~provide powerful tools for examining the influence of inherited topography on present topography and for ~~aiding in the~~ elucidation of tectono-geomorphic histories.

Short summary. Topographic metrics were used to understand topographic changes in response to tectonic activity. We applied metrics to evaluate the relative tectonic activity ~~of~~ along the Ulsan Fault Zone, one of the most active fault zones in Korea. We divided the UFZ into five segments based on spatial variation in activity. We modelled the landscape evolution of study area and interpreted tectono-geomorphic history that the northern part of the UFZ experienced asymmetric uplift, while the southern part did not.

1 Introduction

Research in the field of tectonic geomorphology involves identifying the signal of neotectonic activity from topography. The classic approach to such studies ~~of tectonic geomorphology~~ has traditionally relied on topographic metrics, with origins dating back to the 1900s (e.g., hypsometric integral, stream length–gradient index, and mountain-front sinuosity; Strahler, 1952; Hack, 1973; Bull, 1977; Cox, 1994; Keller and Pinter, 1996; Bull and McFadden, 2020). The normalized channel steepness index (k_{sn}; Flint, 1974; Wobus et al., 2006) and knickpoint analyses are also frequently applied to explore ~~the~~ transient states of channels caused by tectonic activity (Whipple and Tucker, 1999; Duvall et al., 2004; Kirby and Whipple, 2012; Scherler et al., 2014; Marliyani et al., 2016), as channel incision is a direct response to tectonic uplift. The chi (χ) index was introduced to address limitations associated with slope–area analysis for calculating k_{sn}, which can be influenced by (1) noise and errors in topographic data, and (2) the resolution of the data ~~itself~~themselves (Perron and Royden, 2013; Royden and Perron, 2013). Notably, the χ index facilitates straightforward comparison of k_{sn} values across different channel reaches as the slope of the χ–elevation profile directly reflects the k_{sn} value (Perron and Royden, 2013). It ~~is~~ has been applied to determine whether a landscape under specific conditions is in a steady state or transient state, and to assess long-term drainage mobility (Willett et al., 2014; Forte and Whipple, 2018; Kim et al., 2020; Hu et al., 2021; Lee et al., 2021). As computational power has improved and powerful modelling programs have become more widely available, it has become possible to simulate landscape evolution. We can test ~~the~~ site-specific parameters constrained by empirical data (e.g., coefficient of diffusivity, coefficient of fluvial erosion efficiency, and local uplift rate) and determine ~~a~~ ranges of reasonable values through modelling (e.g., Tucker et al., 2001; Braun and Willett, 2013; Goren et al., 2014; Campforts et al., 2017; Hobley et al., 2017; Barnhart et al., 2020; Hutton et al., 2020). ~~It~~Modeling also facilitates the understanding of geomorphic processes and accompanying topographic changes in given tectonic and climatic settings by providing visualisation. These advances have allowed researchers to explain the state (equilibrium or disequilibrium) of ~~the~~ present topography and to predict future landscape evolution within neotectonically active areas (Attal et al., 2011; Reitman et al., 2019; Zebari et al., 2019; Su et al., 2020; He et al., 2021; Hoskins et al., 2023).

Most of the studies mentioned above focus on ~~explaining~~ using ~~how~~ topographic analyses ~~can~~to identify spatial and temporal variations in lithological, tectonic, and climatic conditions. However, ~~these~~such studies do not generally account for the effects of inherited topography (i.e., topography prior to the neotectonic events of interest) on subsequent geomorphic processes, present topographic dynamics, and topographic metrics. We hypothesize that the influence of inherited topography ~~is~~ can be non-negligible in our study area where the fault slip rate is low, and the erosion rate is high, and ~~that~~ topographic metrics ~~reflect the cumulative influence of both past and present geomorphic processes and their drivers~~ would indicate it. Our hypothesis is based on the understanding that: (1) the present topography is a cumulative result of past and present tectonic and climatic events, (2) the response time of geomorphic features such as longitudinal stream profile, knickpoint migration, and divide migration) to the same tectonic events varies (Whipple et al., 2017), and (3) the timescale ~~represented by~~ each topographic metric represents is different and not yet fully understood (Forte and Whipple, 2018). Therefore, we propose that topographic metrics can reflect the cumulative influence of past and present geomorphic processes and their drivers, and that drawing inferences from these indices without accounting for the influence of inherited topography can lead to misinterpretations of landscape evolution.

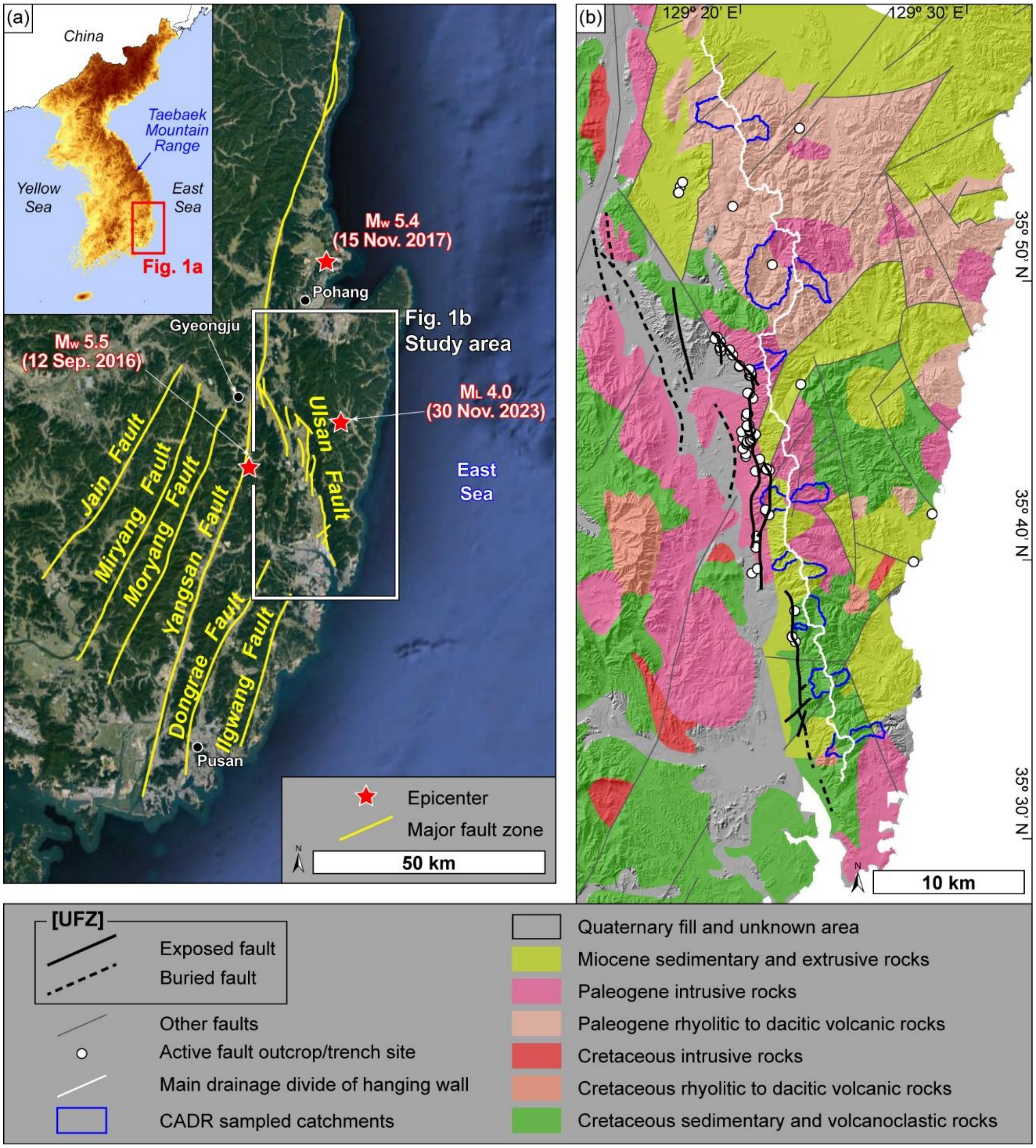

Figure 1: (a) Major fault zones on the southeastern Korean Peninsula (modified from Kim et al., 2016). Our study area is shown by the white box around the Ulsan Fault Zone (UFZ) (base map data: ⓒ 2022 Google, TerraMetrics). (b) Lithology in and around the UFZ (modified from Cheon et al., 2020b, 2023). Exposed faults occur along mountain fronts, and buried faults are located in a wide incised valley west of the mountain range. The hanging wall of the UFZ is on the eastern side of the fault zone and forms the Toham mountain range. The solid white line represents the main drainage divide of the hanging wall (i.e., the eastern block of the UFZ).

In this study, we assess the relative tectonic activity along the UFZ by analysing topographic metrics of the~~for~~ drainage systems associated with the tectonic activity. We then track variations in the topographic metrics along the UFZ to characterize the spatial distribution of the relative tectonic activity and use this information to divide the fault zone into geological segments, following the criteria of McCalpin (1996). Due to ~~the~~ low slip rates, rapid physical and chemical erosion, and extensive urbanisation, it is challenging to find and study ~~the~~clear evidence of neotectonic faulting in Korea. Therefore, assessing the relative tectonic activity using topographic metrics is particularly valuable in the study area. Next, we design several models to simulate the landscape evolution of the study area in response to past and present tectonic activity and compare the topographic metrics from the modelled topographies with those that we analysed for ~~the~~ today's modern study area. Finally, we interpret the influence of inherited topography on the tectono-geomorphic evolution of the study area using the modelling results and topographic metrics, which ~~reflect~~ together potentially record the cumulative influence of past and present geomorphic processes and tectonic activity. We target an area around the Ulsan Fault Zone (UFZ) on the southeastern Korean Peninsula as our study area (Fig. 1). This region is somewhat uniquely poised for studying relationships between geology, tectonics, and geomorphology. Many studies have reported active faults in the UFZ cutting through unconsolidated Quaternary-Holocene sedimentary layers, peat layers, and fluvial terraces (Kyung, 1997; Okada et al., 1998; Cheong et al., 2003; Choi et al., 2012b; Kim et al., 2021). Since these pioneering works, three moderate earthquakes (M_W 5.5 in 2016, M_W 5.4 in 2017, and M_L 4.0 in 2023) have occurred around this area (Fig. 1a), and micro-earthquakes continue to swarm around and on the fault (Han et al., 2017). Studies have also established geological constraints on the boundary conditions for landscape evolution modelling and provided a long-term framework for interpreting the influence of inherited topography on the current landscape and on landscape evolution (Park et al., 2006; Cheon et al., 2012; Son et al., 2015; Kim et al., 2016b; Cheon et al., 2023; Kim et al., 2023a).

2 Study area

Our study area encompasses the UFZ and its hanging wall (i.e., its eastern block). The UFZ is a NNW–SSE- to N–S-striking, east-dipping reverse fault, first identified by the presence of an extensive incised valley and sharp mountain front on the southeastern Korean Peninsula (Fig. 1; Kim, 1973; Kim et al., 1976; Kang, 1979a, b). Although the UFZ has been subject to considerable geological investigation, as it is one of the most active fault zones in Korea, its precise geometry and location and a full understanding of its tectonic history remains elusive. Early studies proposed that the main active strand of the UFZ is located within the incised valley (Kim, 1973; Kim et al., 1976; Kang, 1979a, b). Later studies suggested that it might be within and around the valley, along the mountain front, or even in both locations (Okada et al., 1998; Ryoo et al., 2002; Choi, 2003; Choi et al., 2006; Ryoo, 2009; Kee et al., 2019; Naik et al., 2022). A recent study attempted to comprehensively re-interpret previous studies along with adding new field observations and geophysical data ~~to~~ and proposed a new definition of the UFZ (Cheon et al., 2023). This definition includes some strands of exposed faults along the mountain front and several strands of buried faults near the centre of the incised valley (Fig. 1b). ~~They~~ Cheon et al. (2023) also suggested the UFZ ~~can~~ could be divided into northern and southern segments based on the differences in fault-hosting bedrock~~s~~ and the width of the deformation zone. Accordingly, ~~T~~the northern part of the UFZ consists of Late Cretaceous to Paleogene granitic rock~~s~~ and has a wide deformation zone, ~~while~~ whereas ~~the~~ bedrock ~~of~~in its southern part is composed of Late Cretaceous sedimentary rocks ~~and~~ where ~~the~~ deformation is more focused along ~~the~~ a narrow zone (Cheon et al., 2023).

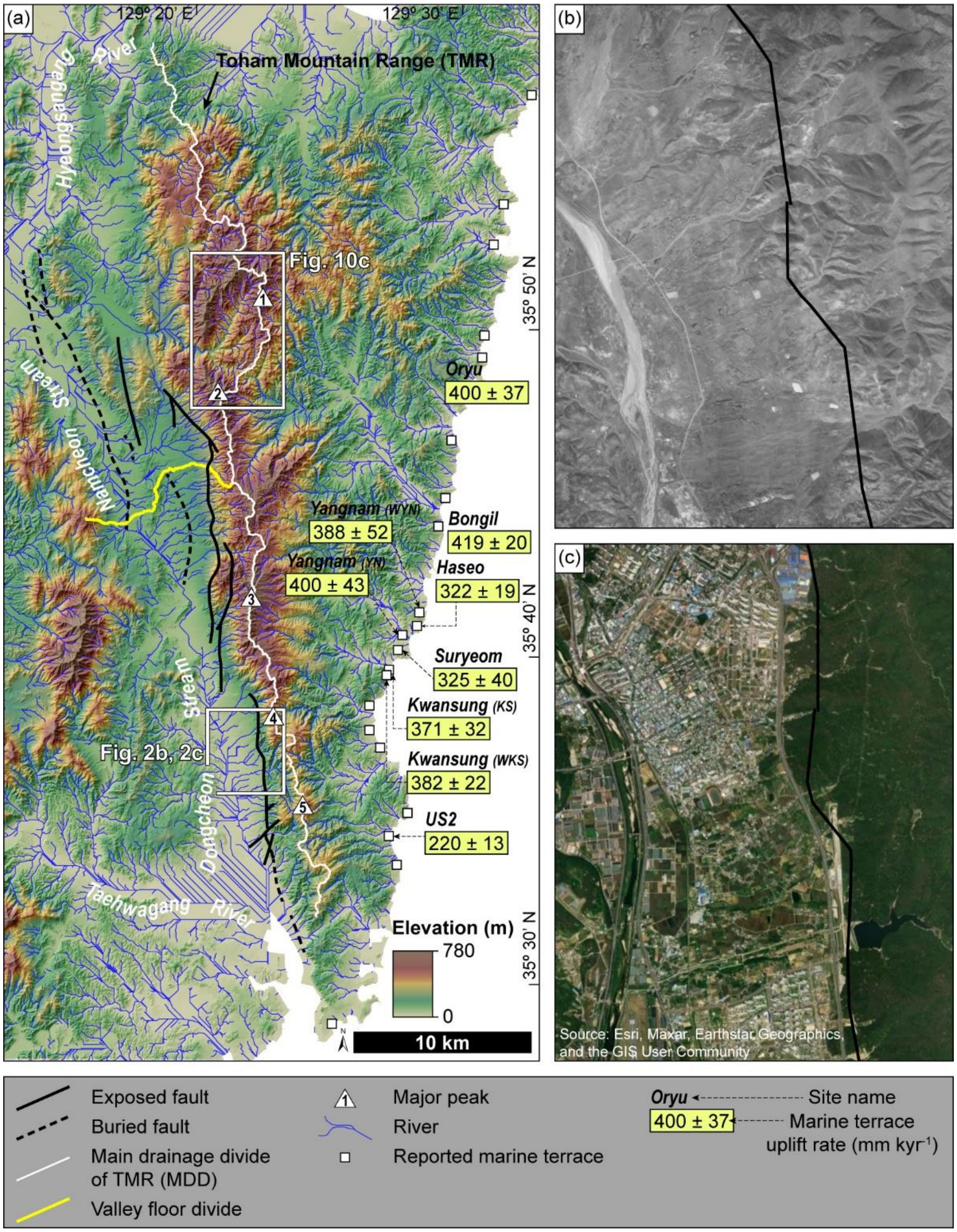

Figure 2: (a) Previously determined uplift rates (in mm kyr^{-1}) of marine terraces near the UFZ, based on the OSL ages of raised beach sediments (details about these rates are in Table 1; Choi et al., 2003a, b; Kim et al., 2007; Heo et al., 2014). The drainage system on the western flank of the Toham Mountain Range (TMR) is divided by the valley floor divide (Namcheon and Dongcheon streams). Major peaks in the eastern block of the UFZ are marked by numbers in white triangles (1: Mt. Hamwol, 2: Mt. Toham, 3: Mt. Gwanmoon, 4: Mt. Dongdae, 5: Mt. Muryong). (b) Aerial photograph taken in 1954 of the area depicted by the white box in Fig. 2a. This aerial photograph was taken prior to urbanisation by the industrial complex and residential district in the study area (image source: National Geographic Information Institute of the Republic of Korea). Alluvial fans extend along the western flank of the mountains. The exposed Ulsan Fault (black line) is traced along the boundary between alluvial fans and the TMR. (c) Recent satellite image (ArcMap^{TM}, ESRI) of the same area as that depicted in Fig. 2b. Urbanisation since the 1960s has made it difficult to observe ~~the~~ natural landforms in this area.

The Toham Mountain Range (TMR) is located on the eastern hanging wall block of the UFZ and extends parallel–subparallel to the fault zone (Fig. 2a). The TMR includes many peaks, including Mt. Hamwol (584 m), Mt. Toham (745 m), Mt. Gwanmoon

(630 m), Mt. Dongdae (447 m), and Mt. Muryong (451 m) from north to south. Rivers draining the TMR are divided into eastern- and western-flank rivers by the main drainage divide (MDD; Fig. 2a). Rivers draining the eastern flank of the TMR flow to the east and drain directly into the East Sea, whereas those on the western flank form a more complex drainage system flowing north or southward from a low-elevation valley floor divide. ~~The w~~Western-flank channels ~~can be divided into northern and southern parts at~~ are categorized based on their draining into the catchments either north or south of the valley floor divide. Channels in the northern part of the valley floor divide flow to the west and join together to form the Namcheon Stream. The Namcheon Stream flows to the north–northwest and joins other tributaries to form the Hyeongsangang River, which drains into the East Sea. Channels in the southern part of the valley floor divide flow to the west and join to form the Dongcheon Stream, which flows to the south. The Dongcheon Stream joins the Taehwagang River, which drains into the Southern Sea of the Korean Peninsula. The landscapes of the western and eastern flanks differ significantly from each other: the western flank is dominated by a clearly defined mountain front with extensive alluvial fans ~~developed along this mountain front~~ (Fig. 2a and 2b), whereas the eastern flank has broader mountainous and hilly landscape that extends from the TMR all the way to the eastern coast (Figs 1a and 2a). The cause of the contrasting landscapes of the western and eastern flanks of the TMR has yet to be unequivocally established, and several explanations have been proposed, including: (1) differential regional rift-margin uplift related to the opening of the East Sea from ca. 20 Ma (Min et al., 2010; Kim et al., 2016a, 2020); (2) differential regional uplift caused by accommodation of the ENE–WSW-oriented neotectonic maximum horizontal stress since 5 Ma (Park et al., 2006; Kim et al., 2016b); and (3) differences in late Quaternary uplift between the western and eastern coasts of the Korean Peninsula, as recorded in marine terraces along the eastern coast (Choi et al., 2003a, b, 2008, 2009; Lee et al., 2015) and shore platform along the western coast (Choi et al., 2012a; Jeong et al., 2021). We weigh in on these possibilities using new data sets in this study.

In addition, numerous studies have attempted to elucidate the geological and geomorphic history of the broader southeastern Korean Peninsula. Studies of the UFZ have reported many active faults (Fig. 1b), but age data from those studies need further verification as at present these results lack consensus (Kyung, 1997; Okada et al., 1998, 2001; Cheong et al., 2003; Kim et al., 2021). Further, studies of marine terraces have proposed paleo-shoreline elevations and the OSL ages of beach-sediment layers for each terrace sequence (Choi et al., 2003a, b; Kim et al., 2007; Heo et al., 2014). In this study, we calculated the amount of uplift of each terrace considering local paleo-sea levels and terrace uplift rates (Table 1 and Fig. 2a).

Table 1: Information on previously studied marine terraces within the study area.

Site name[a]	Latitude (° N, dd)	Longitude (° E, dd)	Paleo-shoreline elevation[b] (m a.s.l.)	Uplift amount[c] (m)	OSL age[d] (ka)	MIS	Uplift rate[e] (mm kyr^{-1})	Reference
Oryu	35.8173	129.5112	26	26	65 ± 6	4	400.00 ± 36.92	(Choi et al., 2003a)
Bongil	35.7301	129.4871	26	26	62 ± 3†	4	419.35 ± 20.29	(Kim et al., 2007)
Yangnam (WYN)	35.6894	129.4708	26	26	67 ± 9	4	388.06 ± 52.13	(Choi et al., 2003b)
Haseo	35.6801	129.4719	45	39	121 ± 7†	5e	322.31 ± 18.64	(Kim et al., 2007)
Yangnam (YN)	35.6774	129.4607	26	26	65 ± 7	4	400.00 ± 43.08	(Choi et al., 2003a)
Suryeom	35.6706	129.4571	45	63	194 ± 24	7	324.74 ± 40.17	(Heo et al., 2014)††
Kwansung (KS)	35.6617	129.4516	26	26	70 ± 6	4	371.43 ± 31.84	(Choi et al., 2003a)
Kwansung (WKS)	35.6580	129.4504	26	26	68 ± 4	4	382.35 ± 22.49	(Choi et al., 2003b)
US2	35.5764	129.4517	18.5	18.2	84 ± 5	5a	220.23 ± 13.11	(Unpublished data)†††

[a] List of sites runs north to south, with some sites sharing names but having different sampling locations (shown in parentheses after each code).

[b] Paleo-shoreline elevation is the present-day elevation of the paleo-shoreline for each terrace.

[c] Uplifted amount is calculated by subtracting the elevation of the sea level at the marine terrace formation from the paleo-shoreline elevation. We considered the elevation of local sea level of each Marine Isotope Stage (MIS) corresponding to each marine terrace age (Lee et al., 2015; Ryang et al., 2022) in our calculations.

[d] Mean ages and 1σ standard deviations are given. These studies used the beach sediment to infer the depositional age.

[e] Uplift rate is calculated by dividing the uplifted amount by the age of marine terrace.

† This age is the average of two samples.

†† This study applied single grain OSL dating method, while the other studies applied single aliquot OSL dating method.

††† Age data is from 'Big Data Open Platform' (https://data.kigam.re.kr/map/) managed by 'Korea Institute of Geoscience and Mineral Resources (KIGAM)'.

3 Methods

3.1 Topographic analysis

We used a 5-m-resolution digital elevation model (DEM) to extract the following topographic metrics: (1) normalised channel steepness index (k_{sn}), (2) stream profiles, (3) metrics for assessing drainage divide mobility, and (4) swath profile. These metrics have been widely used to quantitatively measure topography and geomorphic processes across a diverse range of tectonic and climatic settings. We employed these metrics to assess relative tectonic activity and to delineate ~~geology~~geomorphic-based fault segments, although ~~there are~~ very few additional case studies exist (Lee et al., 2021). The DEM was generated using digital contours provided by the National Geographic Information Institute (NGII) of the Republic of Korea (https://www.ngii.go.kr/kor/main.do; accessed 14 Sep 2020) and was projected to WGS 84 UTM coordinates. We corrected the DEM using ‘carving’ option of TopoToolbox (Schwanghart and Scherler, 2014) for analysis, which ~~decides~~ matches the flow route to the deepest path. ~~The c~~Channel initiation is determined by the threshold drainage area of 10^5 m^2.

3.1.1 Normalised channel steepness index (k_{sn})

~~The bedrock channel incision rate, *E*, can be expressed by Eq. (1), which describes its relationship with channel bed shear stress (Howard and Kerby, 1983; Seidl and Dietrich, 1992; Sklar et al., 1998):~~

$$\cancel{E = KA^mS^n} \qquad \cancel{(1)}$$

~~where *K* is a dimensional coefficient of fluvial erosion efficiency with a unit of [$L^{1-2m}T^{-1}$] encapsulating different controls on erosion, such as rock resistance, climate, bedload sediment grain size, and channel width length relationship (Stock and Montgomery, 1999; Whipple and Tucker, 1999; Snyder et al., 2000; Whipple and Tucker, 2002); *A* [L^2]is drainage area; *S* [L L^{-1}]is the slope; and *m* and *n* are exponents of drainage area and slope, respectively.~~

~~According to Eq. (1), the change in channel elevation (z) with respect to time (t) is:~~

$$\cancel{\frac{dz}{dt} = U - E = U - KA^mS^n} \qquad \cancel{(2)}$$

~~where *U* is rock uplift rate (Whipple and Tucker, 1999; Snyder et al., 2000; Tucker and Whipple, 2002). If the channel adjusts to a tectonic perturbation and thus attains a steady state, then uplift rate and bedrock channel incision rate will balance each other (*dz/dt* = 0), assuming that the bedrock properties and climatic characteristics across the entire channel or catchment are uniform. Then, the~~ The channel ~~can~~ under the steady-state condition in which the uplift, climate, and rock resistance are spatially uniform, maintains a graded profile, following a power-law equation (Hack, 1973; Flint, 1974):

$$S = k_s A^{-\theta} \qquad (1\cancel{3}\text{a})$$

$$S = k_{sn} A^{-\theta_{ref}} \qquad (1\cancel{3}\text{b})$$

where θ is the concavity index of a channel or channel reach ($\theta = m/n$). The channel steepness index (k_s) may be changed by the concavity index, and this makes it difficult to compare values of the channel steepness index with those of other channels with different concavity index values and different sizes of drainage basins. To facilitate such a comparison, the normalised channel steepness index (k_{sn}) can be calculated by fixing the concavity index with a reference value (θ_{ref}) in the range of 0.36–0.65 (Snyder et al., 2000; Wobus et al., 2006; Cyr et al., 2010; Kirby and Whipple, 2012). However, many streams in nature are not graded, particularly if they have undergone base-level changes that resulted from climate change (Crosby and Whipple, 2006), tectonic forcing (Snyder et al., 2000; Kirby and Whipple, 2001), or lithological differences (Cyr et al., 2014). Such streams show peaks or piecewise-fitted lines in a log *S*–log *A* plot and display abrupt variation in k_{sn} along their course, indicating that they are in a geomorphic transient state. We computed k_{sn} as the derivative of χ and elevation as noted by Eq. (~~4~~2a) with θ_{ref} of 0.45, using LSDTopoTools (Mudd et al., 2014). To validate the use of empirical value we use, we calculated concavity indices across the study area, which range from 0.36 to 0.47. Therefore, we believe that using 0.45 as θ_{ref} should not pose any major issues.

3.1.2 Stream profile analysis and knickpoint extraction

According to Eq. (1~~3~~a), a graded stream has a concave longitudinal profile and is represented as a single line on a log *S*–log *A* plot. The χ-transformed stream profile of a graded stream (χ–z plot) also would be represented by a single line, based on Eq. (2~~4~~a). However, rivers in transient states are expected to show several piecewise linear segments in a χ-transformed stream profile (Perron and Royden, 2013). The boundary between adjacent piecewise lines can be identified as a knickpoint, which is a part of a channel with an abrupt change in slope and elevation of channel bed. A knickpoint can reflect the transient state of a stream that is caused by a base-level change related to climatic change (Crosby and Whipple, 2006), tectonic forcing (Snyder et al., 2000; Kirby and Whipple, 2001), or lithological difference (Cyr et al., 2014).

We used TopoToolbox (Schwanghart and Scherler, 2014) to extract the longitudinal stream profiles. To visualize the changes in the normalised channel steepness index values more easily, we extracted χ-transformed stream profile, using LSDTopoTools (Mudd et al., 2014). This tool employs an algorithm to analyse the best fitting piecewise line for each channel segment (Mudd et al., 2014).

We set the reference concavity index (θ_{ref}) to 0.45 and the reference scaling area (A_0) to unity for integral transformation of χ the coordinate.

3.1.3 Metrics for assessing drainage divide mobility

~~The~~ Drainage divide mobility is determined by the contrasts in erosion rates of adjacent drainage basins. As the erosion rates depend on topography, we can use topographic metrics to assess the divide mobility and drivers of divide migration. We used the mean upstream relief which is the most reliable metrics among the Gilbert metrics (Forte and Whipple, 2018) and the χ index to evaluate topographic asymmetry and divide mobility. This is based on the ‘law of divides’ of Gilbert (1877), which suggested that the steeper slope is expected to be eroded and reduced in height more rapidly when compared with the gentle slope (Fig. 70 in Gilbert, 1877). The migration will in principle continue until the two sides become symmetric (geometric equilibrium) (Gilbert, 1877). In addition to these metrics, the chi (χ) index at opposing channel heads can also be used to evaluate long-term divide stability (Willett et al., 2014; Forte and Whipple, 2018). The χ index at a point x on the channel serves as a proxy for the steady-state elevation of the channel and is calculated by integrating Eq. (1~~3~~b) from downstream to upstream (Perron and Royden, 2013):

$$z(x) = z_b + \left(\frac{k_{sn}}{{A_0}^{\theta_{ref}}}\right)\chi \tag{\cancel{4}2a}$$

$$\chi = \int_{x_b}^{x} \left(\frac{A_0}{A(x')}\right)^{\theta_{ref}} dx' \tag{\cancel{4}2b}$$

where x is the distance upstream from an arbitrary base-level, z_b is a base-level elevation (at $x = x_b$), A_0 is an arbitrary scaling area, and $A(x)$ is the drainage area at point x on the channel. The integrand in Eq. (2~~4~~b) becomes dimensionless, meaning that the χ index can be expressed with a unit of length (Perron and Royden, 2013). Equation (2~~4~~a) establishes the linear relationship between the elevation and the χ index when the rock uplift, bedrock erodibility, and climate conditions are invariant along the channel, and the χ index is calculated with the adequate θ_{ref}. If such boundary conditions spatially vary, the elevation and χ index will have piecewise-linear relationship. The scaling area, A_0, is set to unity, as the slope of the χ index–channel elevation plot (χ–z plot) is equal to k_{sn}, based on Eq. (2~~4~~a). We used TopoToolbox (Schwanghart and Scherler, 2014) and DivideTools (Forte and Whipple, 2018) to analyse mean upstream relief and the χ index. The mean upstream relief is calculated within ~~the~~ a radius of 200 m, which was determined by considering the resolution of topographic data and the distance between the channel head and MDD. Finally, because the χ index is sensitive to the base-level elevation (z_b; Forte and Whipple, 2018), we analysed the χ index with two different base-level elevations (50 and 200 m). The drainage basins with base-level elevations lower than 50 m and higher than 200 m do not adequately to describe the variation of topographic metrics along the UFZ. For these basins, ~~W~~we ~~then~~ performed Student's t-test which is a statistical method to determine whether two groups are statistically significantly different from each other. We applied this Student's t-test (two-tailed, α = 0.05) to statistically compare the values of these topographic metrics between the western and eastern flanks of the TMR.

3.1.4 Swath profile

Swath profiles quantify how minimum, mean, and maximum elevation varies across a region along a profile. ~~It~~ They have provend useful~~can be used~~ to understand the relationship between surface topography (i.e., swath profile) and associated or causative variables, such as dynamic topography, which is a topographic change caused by mantle convection (Stephenson et al., 2014), or spatial patterns of precipitation (Bookhagen and Burbank, 2006), and uplift and exhumation rates (Taylor et al., 2021). We extracted a swath profile along the MDD and set the width to 3 km using TopoToolbox (Schwanghart and Scherler, 2014), as along-strike topographic variation is expected to be related to the along-strike variation in the cumulative vertical displacement on the UFZ.

3.2 In situ cosmogenic ^{10}Be measurements

Assuming that the channel of interest approaches a topographic steady state where the channel bed maintains constant elevation due to the balance between uplift and incision, uplift rate can be derived from the bedrock channel incision rate [Eqs. (1) and (2)]. We used *in situ* cosmogenic ^{10}Be measurements to constrain the catchment-averaged denudation rate and bedrock channel incision rate to quantify the uplift rate and the stream power variation controlled by tectonic uplift in the study area.

3.2.1 Catchment-averaged denudation rate

The concentration of *in situ* cosmogenic ^{10}Be from riverine sediment on the present bedrock channels can be interpreted as the catchment-averaged denudation rate (CADR). This approach assumes a geochemical steady state whereby the production and removal (via denudation) rates of cosmogenic ^{10}Be within the catchment are equal (Brown et al., 1995; Bierman and Steig, 1996; Granger et al., 1996; von Blanckenburg, 2005). Thus, the CADR represents the average denudation rate across the entire catchment by hillslope and fluvial processes over a given integration time, during which the sediments remained within the catchment (Granger et al., 1996; von Blanckenburg, 2005). The integration time documented in previous studies from a variety of tectonic, climatic, and topographic environments varies from 10^3 to 10^6 years (Brown et al., 1995; DiBiase et al., 2010; Portenga et al., 2015; Kim et al., 2020).

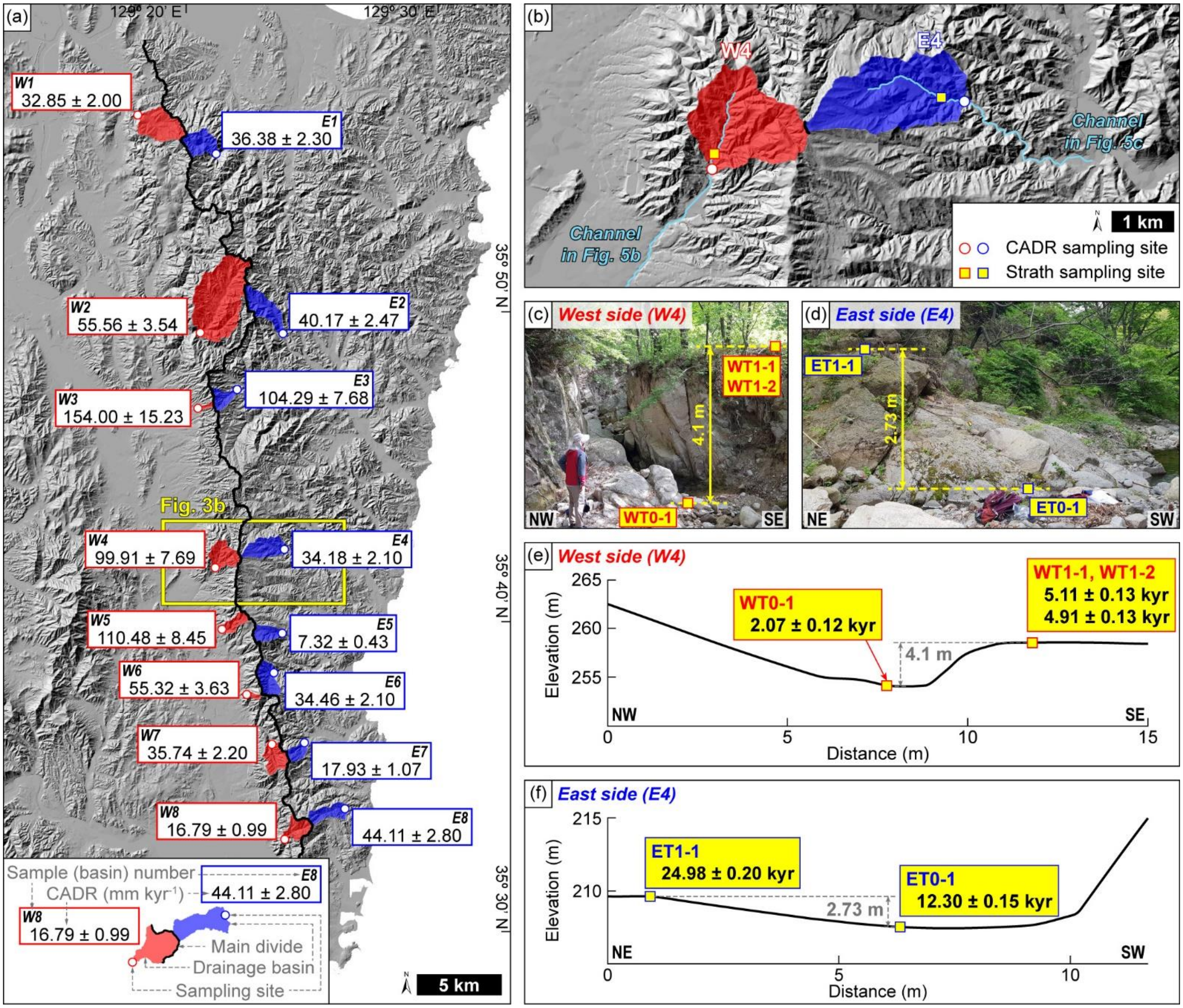

Figure 3: Sampling sites and results of catchment-averaged denudation rates (CADRs) and channel incision rates derived from *in situ* cosmogenic ^{10}Be measurement. (a) CADRs calculated using *in situ* cosmogenic ^{10}Be measurements and their sampling sites. We collected samples for ^{10}Be analysis and CADR calculation from eight pairs of basins (16 basins) along the main drainage divide. CADR values on the western flank of the TMR (shown in red) are mostly higher than those on the eastern flank (shown in blue). (b) Bedrock strath sampling sites, where channel profiles are provided in Figs. 5b and 5c, are marked. (c and d) Photographs of the bedrock strath sampling sites on the western and eastern flanks of the TMR, respectively. We collected samples from the bedrock strath and the present stream bed in the same catchments from which we collected samples W4 and E4 for CADR calculation. The height of the western-flank strath above the present stream bed is 4.1 m, and the height of the eastern-flank strath above the present stream bed is 2.73 m. (e and f). Elevation profiles across the bedrock strath sampling sites and their ^{10}Be exposure ages on the western and eastern flanks of the TMR, respectively. The age difference between the present stream bed and the strath is 2.94 ± 0.15 kyr on the western flank and 12.68 ± 0.25 kyr on the eastern flank. The discrepancy between CADR and bedrock channel incision rate is tentatively caused by (1) the difference between the integration time of CADR and the exposure age of strath surface and (2) the difference of spatial scales which is represented by those two methods.

We collected 16 samples of riverine sediment from eight pairs of catchments (a total of 16 catchments) straddling both sides of~~along~~ the MDD of the TMR (Fig. 3a) to document variations in the CADR along the MDD. More specifically~~over~~, we aim to compare the CADRs of the western and eastern flanks of the TMR to reveal the direction of divide migration and tectono-geomorphic history of the hanging wall and footwall blocks. The along-MDD variation and across-MDD contrasts were subsequently compared with results from our topographic analysis to characterise the tectonic activity and its spatial variability along the UFZ. We obtained samples of fine- to medium-grained sand (250–500 μm) from channel beds. To prevent possible contamination by anthropogenic debris, we avoided collecting samples from catchments containing golf courses and downstream areas where alluvial fans are located, and faults occur (Fig. 2).. The lithology of the sampled catchments includes mainly sedimentary rocks and igneous rocks of various geological ages (Fig. 1b). The lithology within each pair of basins (basins contacting at the MDD, such as basins W1 and E1 in Fig. 3a) is, however, highly similar, ensuring minimal influence of lithological difference on CADRs for comparison in the across-MDD direction. However, some lithological variations do occur in the along-MDD direction. The basins W1 and E1 consist of rhyolite and dacite bedrock. Basins W2, W3, E2, and E3 contain rhyolite, dacite, and granite bedrock as shown in Fig. 1b. The remaining basins (W4−W8 and E4−E8; eight basins) contain sedimentary, volcanoclastic, and granite bedrock.

We performed chemical treatment of the CADR samples at Korea University, Seoul, South Korea, following a standard protocol for ^{10}Be extraction (Kohl and Nishiizumi, 1992; Seong et al., 2016). We leached the samples with an HCl–HNO_3 mixture to remove organic and carbonate materials. Then, we used an HF–HNO_3 mixture to remove minerals other than quartz and meteoric ^{10}Be adsorbed onto the surface of mineral particles. An amount of 15–20 g of pure quartz was yielded after separating magnetic minerals and picking out other impurities. A ^{9}Be carrier with a low background level of ^{10}Be was then added to the samples, which were then dissolved with a high-concentration HF–HNO_3 mixture. We extracted beryllium using an ion-exchange column, precipitated it into BeOH, dried the BeOH gel, and calcined it into BeO. The samples in BeO form were mixed with niobium powder and targeted into the cathode. Accelerator mass spectrometry measurements were performed at the Korea Institute of Science and Technology (KIST), Seoul, South Korea. Measured ^{10}Be/^{9}Be results were normalised to the 07KNSTD reference 5-1 sample (Nishiizumi et al., 2007) and calculated as ^{10}Be concentrations after correction with a process blank ($4.37–4.53 \times 10^{-15}$; $n = 6$).

We utilised the BASINGA (basin average scaling factors, cosmogenic production, and denudation rates) tool (Charreau et al., 2019) to calculate CADRs and integration time from ^{10}Be concentrations. This tool calculates the basin-averaged production rate of *in situ* cosmogenic ^{10}Be from every cell of a DEM based on its location. The tool requires raster files of a DEM and offers scaling schemes of Lal/Stone (Lal, 1991; Stone, 2000), LSD, and LSDn (Lifton et al., 2014), along with geomagnetic correction based on the virtual dipole moment (Muscheler et al., 2005). We used the same topographic data for calculating CADRs as we did for topographic analysis, employing a 5-m-resolution DEM derived from digital contours of NGII. Additionally, we applied the LSDn scaling scheme (Lifton et al., 2014) and geomagnetic correction (Muscheler et al., 2005).

3.2.2 Bedrock channel incision rate

The classical model of fluvial strath terrace formation includes the widening of the terrace tread by lateral erosion and its abandonment by incision (Burbank and Anderson, 2011). Each abandoned terrace represents the position of the paleo-channel of the stream bed, and bedrock incision is controlled by uplift, as channels incise bedrock while they attain steady state ~~[Eq. (2)]~~. If the concentration of *in situ* cosmogenic ^{10}Be on a strath surface can be measured, then the exposure age of that bedrock strath can be calculated, indicating the time elapsed after abandonment of the strath surface.

We collected three samples from western-flank straths and two from eastern-flank straths (Fig. 3) to constrain the exposure age of each tread. The sampled strath terraces are located in the drainage basin from which the W4 and E4 CADR samples were taken. All terraces consist of granite bedrock. The height of the strath terrace from the channel bed on the western flank was 4.10 m, and that on the eastern flank was 2.73 m (Figs. 3c–3f). On the western flank, the valley is deep and narrow, and the valley wall is steep. On the eastern flank, the valley is wide and gentle, and the exposed valley wall and terrace riser are more weathered than those on the western flank. The terraces in both valleys are unpaired.

Following the same laboratory protocol described above (Kohl and Nishiizumi, 1992; Seong et al., 2016), we performed physical and chemical treatment for *in situ* surface exposure dating samples at Korea University, Seoul, South Korea. We crushed bedrock samples using a jaw crusher and iron mortar and separated fine- to medium-sized sand (250–500 µm) grains by sieving. The further chemical treatments were the same as those applied to our CADR samples (see section 3.2.1 above). AMS measurements were made at Korea Institute of Science and Technology (KIST), Seoul, South Korea. We calculated exposure ages using the CRONUS-Earth online calculator (Balco et al., 2008; version 3.0.2), applying the LSDn scaling scheme (Lifton et al., 2014). Uncertainties of exposure ages were calculated and are given as 1σ values.

3.3 Landscape evolution modelling

We applied the open-source landscape evolution model toolkit 'Landlab' (Hobley et al., 2017; Barnhart et al., 2020; Hutton et al., 2020) to investigate the specific landscape evolution model setups to get insights about the evolution of the uplifted eastern hanging wall block of the UFZ. These simulations were then compared with results from topographic analyses and ^{10}Be measurements to interpret the landscape evolution of the study area. We considered two processes that erode topography and transport sediment: (1) fluvial erosion and (2) hillslope diffusion.

The bedrock channel incision rate, E, can be expressed by Eq. (3), which describes its relationship with channel bed shear stress~~Topographic change caused by fluvial erosion is controlled by the stream power incision law~~ (Howard and Kerby, 1983; Seidl and Dietrich, 1992; Sklar et al., 1998).~~, following Eq. (1).~~

$$E = KA^m S^n \qquad (3)$$

where K is a dimensional coefficient of fluvial erosion efficiency with a unit of $[L^{1-2m}T^{-1}]$ encapsulating different controls on erosion, such as rock resistance, climate, bedload sediment grain size, and channel width length relationship (Stock and Montgomery, 1999; Whipple and Tucker, 1999; Snyder et al., 2000; Whipple and Tucker, 2002); A $[L^2]$ is drainage area; S $[L\ L^{-1}]$ is the slope; and m and n are exponents of drainage area and slope, respectively. We used values of K = 5.56E-07 $m^{-1.29}$ yr^{-1}, m = 1.1448, and n = 2.2896 to simulate fluvial erosion, which was estimated by averaging values calculated for regions with similar lithology, climate, and tectonic activity to those of our study area (Harel et al., 2016). We applied an incision threshold of 1.0E-05 m yr^{-1}, below which no incision is assumed to occur (Tucker and Whipple, 2002; Harel et al., 2016; Hobley et al., 2017).

Topographic change caused by hillslope diffusion is controlled by the diffusion equation (Culling, 1963; Tucker and Bras, 1998):

$$\frac{\partial z}{\partial t} = K_d \nabla^2 z \qquad (4\cancel{5})$$

where K_d is the coefficient of diffusivity with a unit of $[L^2\ T^{-1}]$; ∇^2 is the Laplace operator, which is the divergence of gradient; and z is elevation. We used K_d = 0.001 to simulate the hillslope diffusion process, which we adopted because soil is rare on slopes (Fernandes and Dietrich, 1997; Zebari et al., 2019).

The landscape gain in height by tectonic uplift and loss of height by fluvial erosion and hillslope diffusion can be expressed as (Temme et al., 2017):

$$\frac{\partial z}{\partial t} = U - KA^m S^n - K_d \nabla^2 z \qquad (5\cancel{6})$$

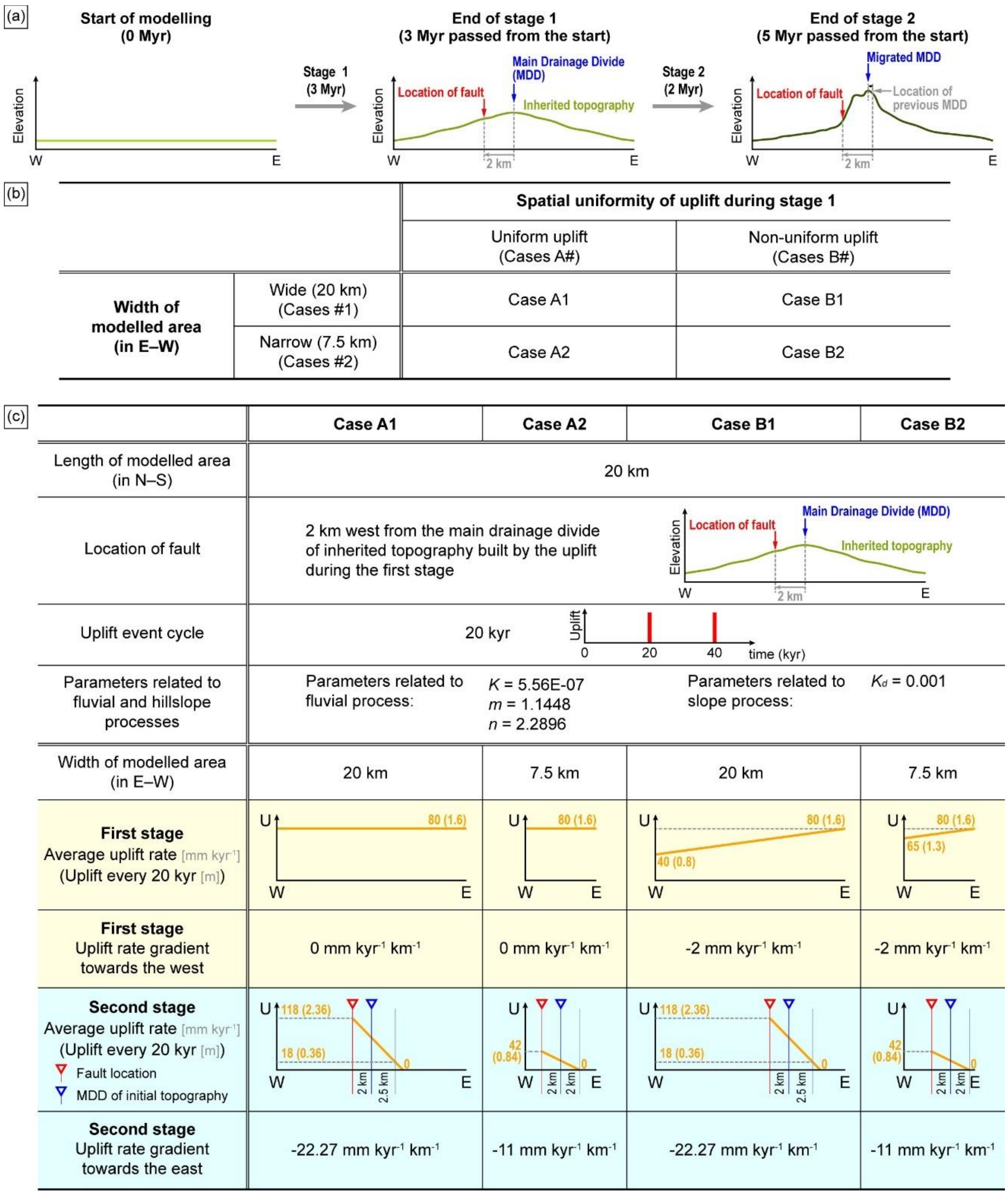

Figure 4: Diagram showing configuration of the landscape evolution model (LEM) used to simulate the tectono-geomorphic evolution of the eastern hanging wall block of the UFZ. (a) The two stages of the LEM. The stage 1, corresponding to a duration of 3 Myr, involves simulation of building of the initial topography; i.e., the topography prior to reverse faulting of the UFZ during the Plio-Quaternary. The stage 2, corresponding to a duration of 2 Myr, involves simulation of reverse faulting and associated neotectonic surface uplift on the UFZ during the Quaternary. We modelled the location of the fault in the LEM as being 2 km west of the average location of the main drainage divide (MDD) of the initial topography. (b) The four model cases (A1-A2, B1-B2) used to test different conditions of spatial uniformity/non-uniformity of uplift during stage 1 and the width of the modelled domain. (c) Detail settings for each case (A1-A2, B1-B2) of the LEM. The settings in the first four rows of this table are universal to all four cases. We applied different uplift rates and spatial gradients in uplift during both stages 1 and 2 for each case. 'U' means average uplift rate (in a unit of mm kyr^{-1}), 'W' means the western boundary of the eastern block of the UFZ, and 'E' means the eastern boundary of the eastern block of the UFZ. The numbers in the parentheses represent the uplift amounts at every 20 kyr (i.e., one uplift event cycle). Model uplift rate during stage 1 for Cases A1 and A2 is spatially uniform, whereas that for Cases B1 and B2 is spatially variable, decreasing linearly from east to west. In the second-to-bottom row of the table, the red triangle denotes the location of the fault, and the blue triangle marks the location of the MDD of initial topography. The uplift rate during stage 2 decreases linearly with increasing distance from the fault. The uplift rates and their spatial gradient during stage 2 depend on the width of the modelled domain. Cases #1 share the same uplift rate and its spatial gradient, and Cases #2 have the same values for the uplift rate and its spatial gradient.

We designed the landscape evolution model to incorporate two stages: the first to establish the inherited topography and the second to simulate the fault movement (Fig. 4a). By applying different boundary conditions during the first stage (Fig. 4b), we could simulate various inherited topographies. This approach allowed us to test our hypothesis that the inherited topography significantly influences the present landscape and the patterns of topographic metrics. The first stage is a pre-Quaternary period during which initial topography is built; i.e., the topography that already existed before reverse faulting of the UFZ during the Quaternary. This period simulates the regional uplift prior to the Quaternary reverse faulting of the UFZ. The second stage is a period in which to simulate local uplift by reverse faulting, representing neotectonic movement of the UFZ during the Quaternary. In the model, we structured stage 1 to last for 3 Myr and stage 2 to last for 2 Myr, giving a total time of 5 Myr. The total duration corresponds to the duration of the present stress regime, as the regional and local uplift both occurred under the present stress regime (Park et al., 2006; Kim et al., 2016b).

With this model structure, we tested four cases differentiated by varying two parameters: (1) spatial uniformity of uplift rate in the first stage, and (2) the width of the modelled domain (Fig. 4b). First, the cases can be separated into two groups (A and B) based on the spatial uniformity of uplift rate during stage 1. The cases simulating a spatially uniform uplift rate during stage 1 (henceforth 'Cases A#') assume that there was no spatial gradient in uplift rate, namely, that the whole eastern block of the UFZ underwent uniform uplift during stage 1. The cases simulating a spatially variable uplift rate during stage 1 (henceforth 'Cases B#') assume that there was a spatial gradient in uplift rate whereby the eastern side of this block was uplifted more than the western side (i.e., the modelled domain tilted westward). This assumption is based on the overall tendency of high-east and low-west topography of the Korean Peninsula, supported by the long-term, regional westward tilting that was initiated during the Middle Miocene when the East Sea started to widen, and since which time the strongly asymmetric (high-east) Taebaek Mountain Range has been rapidly uplifted (Min et al., 2010; Kim et al., 2020). In addition, the shore platform on the western coast of the peninsula (0 m a.s.l.; Choi et al., 2012a; Jeong et al., 2021) and marine terraces along the eastern coast (18–45 m a.s.l.; Choi et al., 2003a, b; Kim et al., 2007; Heo et al., 2014; Lee et al., 2015), formed at the same time (i.e., during MIS 5), indicate that this regional differential uplift of the entire peninsula has lasted until very recently. Second, we divided the cases into two groups (henceforth 'Cases #1 and #2') based on the width of the modelled domain (Fig. 4b) to simulate the observation that the eastern block of the UFZ is wide in its northern part and narrows towards the south (Fig. 1). The width of the wide-modelled domain (measured in an E–W direction) is 20 km (henceforth 'Cases #1'), and that of the narrow-modelled domain (henceforth 'Cases #2') is 7.5 km, so that Cases #1 and Cases #2 represent the northern and southern parts of the block, respectively.

In all four cases, we employed identical values for the following settings and parameters: (1) the length of the modelled domain in the N–S direction; (2) the location of the fault; (3) the parameters used to simulate fluvial and hillslope processes; and (4) the uplift event cyclicity (Fig. 4c). The N–S length of the modelled domain was set to 20 km for all cases. We positioned the model Ulsan Fault 2 km west of the average location for the MDD of the initial topography (Figs. 4a and 4c). This was done because the present-day location of the UFZ is approximately 2 km west of the MDD of the eastern block. The three parameters associated with fluvial process: the coefficient of erosion (K) and exponents of area (m) and slope (n), and the one parameter associated with slope processes; i.e., the coefficient of diffusivity (K_d; as described above; Fig. 4c) were set to constants. Finally, we set the uplift event cyclicity (i.e., the duration between discrete faulting and uplift events) to 20 kyr. Although the earthquake recurrence interval has not yet been definitively determined for the Ulsan Fault, we used a realistic value based on the correlation between earthquake magnitude, recurrence interval, and geomorphic evidence proposed by Slemmons and Depolo (1986), as well as the timing of the most recent and penultimate earthquakes in the study area (Cheon et al., 2020a; Kim et al., 2023b).

We applied different average uplift rates and their spatial gradients during both stages for the individual~~particular~~ cases we explore (Fig. 4c). The average uplift rates during stage 1 for Cases A1 and A2 were spatially uniform (i.e., no spatial gradient). The average uplift rate for Cases A# during stage 1 was set to 80 mm kyr^{-1}. This value was chosen to set our model uplift rate to be the same as the long-term (from 22 Ma until today) exhumation rate across the Taebaek Mountain Range (the "backbone" mountain range of the Korean Peninsula) since 22 Ma (Han, 2002; Min et al., 2010; Kim et al., 2016a). Conversely, Cases B1 and B2 incorporate a spatial gradient in uplift rate, with the highest uplift rate in the east, decreasing gradually towards the west during stage 1. Although the spatial gradient of uplift rate is uncertain, we chose to model the average uplift rate at the western margin of the domain in Case B1 (40 mm kyr^{-1}) as half of the maximum uplift rate at the eastern margin (80 mm kyr^{-1}), which is equivalent to the uplift rate of Cases A# during stage 1 (Fig. 4c). The same spatial gradient in uplift rate (-2 mm kyr^{-1} km^{-1}) was applied in Case B2.

During stage 2 (Quaternary reverse faulting), the average uplift rate is set to be the highest at the location of the fault and to diminish linearly with increasing distance from the fault. To determine the maximum vertical displacement per event, we assumed that a maximum earthquake magnitude of M_W 7.0 occurs once per 20 kyr (Slemmons and Depolo, 1986; Kyung, 2010), although different maximum magnitude estimates (M_W 4.6–5.6) have been proposed for the Ulsan Fault (Choi et al., 2014). According to the empirical equation of Moss and Ross (2011), a M_W 7.0 earthquake would generate a maximum vertical displacement of approximately 2.36 m. Therefore, we hypothesised a scenario in which a M_W 7.0 earthquake produces a maximum vertical displacement on the fault of 2.36 m every 20 kyr. Under this scenario, the average long-term surface uplift rate at the fault location for Cases #1 is 118 mm kyr^{-1} (0.118 mm yr^{-1}) as calculated by dividing the maximum vertical displacement (2.36 m) by 20 kyr (Fig. 4c). This rate decreases linearly to 18 mm kyr^{-1} (0.018 mm yr^{-1}) at a distance of 2.5 km east of the MDD of the initial topography. This value (18 mm kyr^{-1}) is calculated by multiplying the average uplift rate at the fault location (118 mm kyr^{-1}) by the ratio of the eastern-flank channel incision rate (215 mm kyr^{-1}) to that in the west (1394 mm kyr^{-1}). This calculation reflects the fact that the sampled western-flank strath is located ~2 km west of the UFZ, and the eastern-flank strath we sampled is ~2.5 km from the MDD. For Cases #2, representing the southern part of the block, we applied a lower average uplift rate of 42 mm kyr^{-1} (0.042 mm yr^{-1}) at the fault location (Fig. 4c). We used this lower uplift rate because CADRs in the southern part of the study area are lower than those in the northern part (Table 2 and Fig. 3a). This uplift rate (42 mm kyr^{-1}) was calculated by multiplying the ratio of the average CADR of W6–W8 (36.25 mm kyr^{-1}) to the CADR of W4 (100.56 mm kyr^{-1}) by 118 mm kyr^{-1}. This choice in parameterization reflects that the western-flank strath terrace is located within the drainage basin from which we collected the W4 CADR sample. The uplift rate becomes zero 2 km east of the MDD because most of the knickpoints on the eastern-flank channels in the southern part of the study area are located within 2 km of the MDD (Fig. 5a).

Each of the four landscape evolution model cases has a grid spacing of 100 m. We traced the change in topography development using a time-step of 100 yr. Comparisons between the resultant topographies from Case A1 to Case B1 and from Case A2 to Case B2 allow us to detect the influence of inherited topography (i.e., topography achieved after stage 1) on the subsequent geomorphic response to the same pattern of tectonic movement (i.e., uplift by faulting during stage 2). Similarly, comparisons of the resultant topographies from Case A1 to Case A2 and from Case B1 to Case B2 enable us to detect the differential geomorphic response controlled by differences in the width of the modelled domain or in channel length. In addition, our model results can be used to compare our results obtained from topographic analysis, CADRs, and channel incision rates calculation from ^{10}Be measurement, as these were used as inputs for the simulation. We analysed mean upstream relief and the χ index for the modelled topographies using TopoToolbox (Schwanghart and Scherler, 2014) and DivideTools (Forte and Whipple, 2018) to quantitatively compare the topographies generated in the four cases.

4 Results

4.1 Topographic analysis

4.1.1 k_{sn} and knickpoint analyses on stream profiles

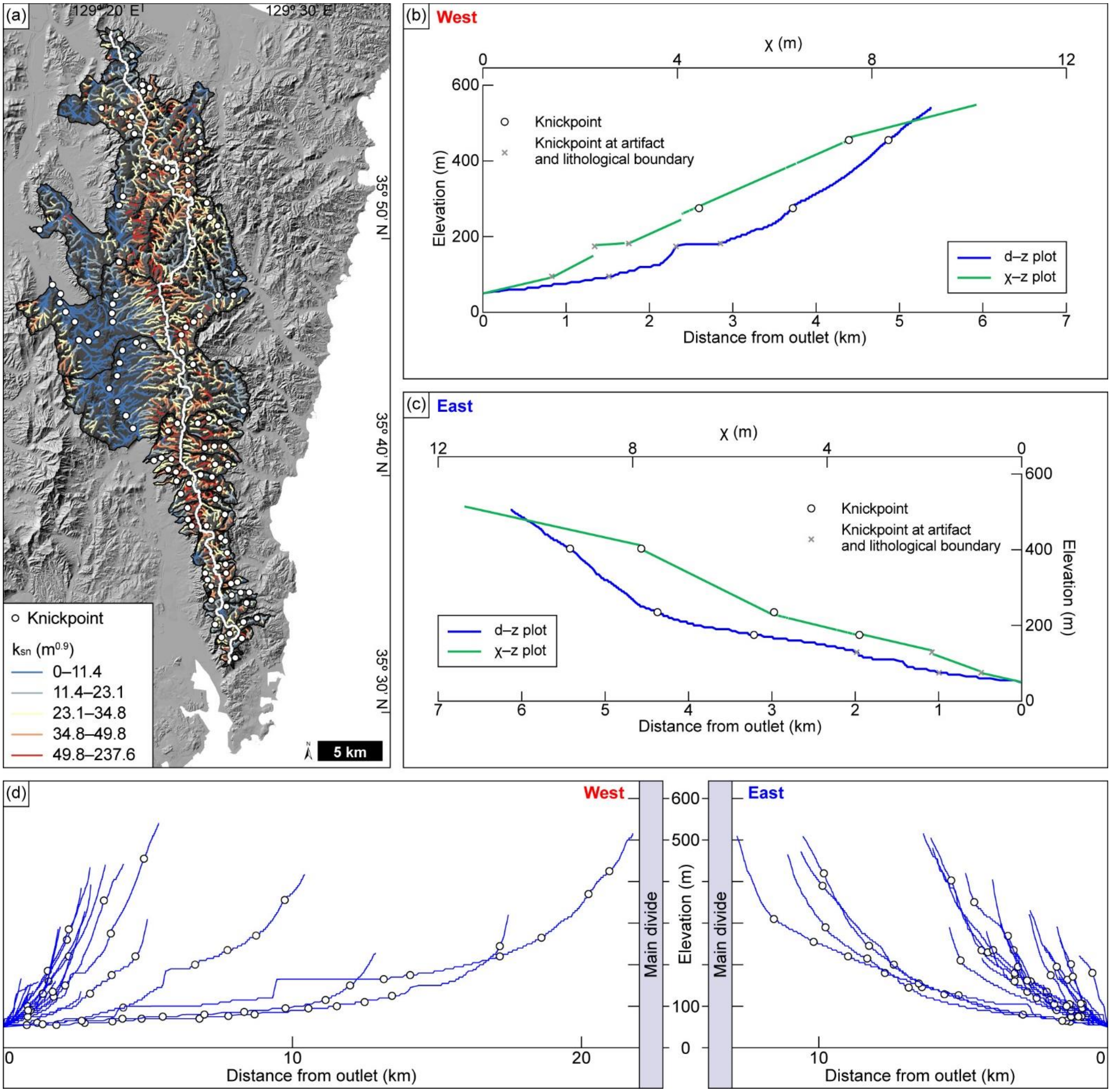

Figure 5: (a) Spatial distribution of knickpoints on trunk stream channels and map of normalised steepness index (k_{sn}) for the entire study area. A reference concavity index (θ_{ref}) of 0.45 was applied to calculate values of k_{sn}. Knickpoints (white circle) were detected after excluding artefacts and lithological boundaries. (b and c) Plots of *d*–*z* (blue) and *χ*–*z* (green) for a stream on each of the western and eastern flanks, respectively, where *d* is distance from the outlet and *z* is elevation. Knickpoints detected at artefacts and lithological boundaries are marked with grey crosses. The locations of these channels are marked in Fig. 3b. (d) Longitudinal profiles and knickpoints of all trunk channels in the study area. Knickpoints detected at the artefacts and lithological boundaries are excluded.

We find that k_{sn} varies from 0 to 238 $m^{0.9}$, with a regional mean of 24 $m^{0.9}$ and a standard deviation of 16 $m^{0.9}$. Values lower than the regional mean k_{sn} are observed in the lowlands of the incised valley on the western flank. Values higher than the regional mean k_{sn} appear from the foothills of the mountain range. Analyses of k_{sn} and knickpoints on the longitudinal and χ-transformed stream profiles show that the channels on both (western and eastern) sides are in a transient state (Fig. 5). This result implies that these channels have been disturbed either by lithologies with different K values or by base-level change. We manually excluded artefact knickpoints (e.g., known anthropogenic features such as dams and reservoirs) and lithological boundaries by examining satellite images and geological maps and performing checks in the field. The remaining knickpoints can be interpreted as being caused by tectonic events, and are in accordance with the findings of a previous study (Kim et al., 2016a), which suggested on the basis of a 1-D model that the observed major knickpoints in the study area cannot have been formed by sea level changes since the global Last Glacial Maximum.

4.1.2 Variations in values of topographic metrics in the along- and across-MDD directions

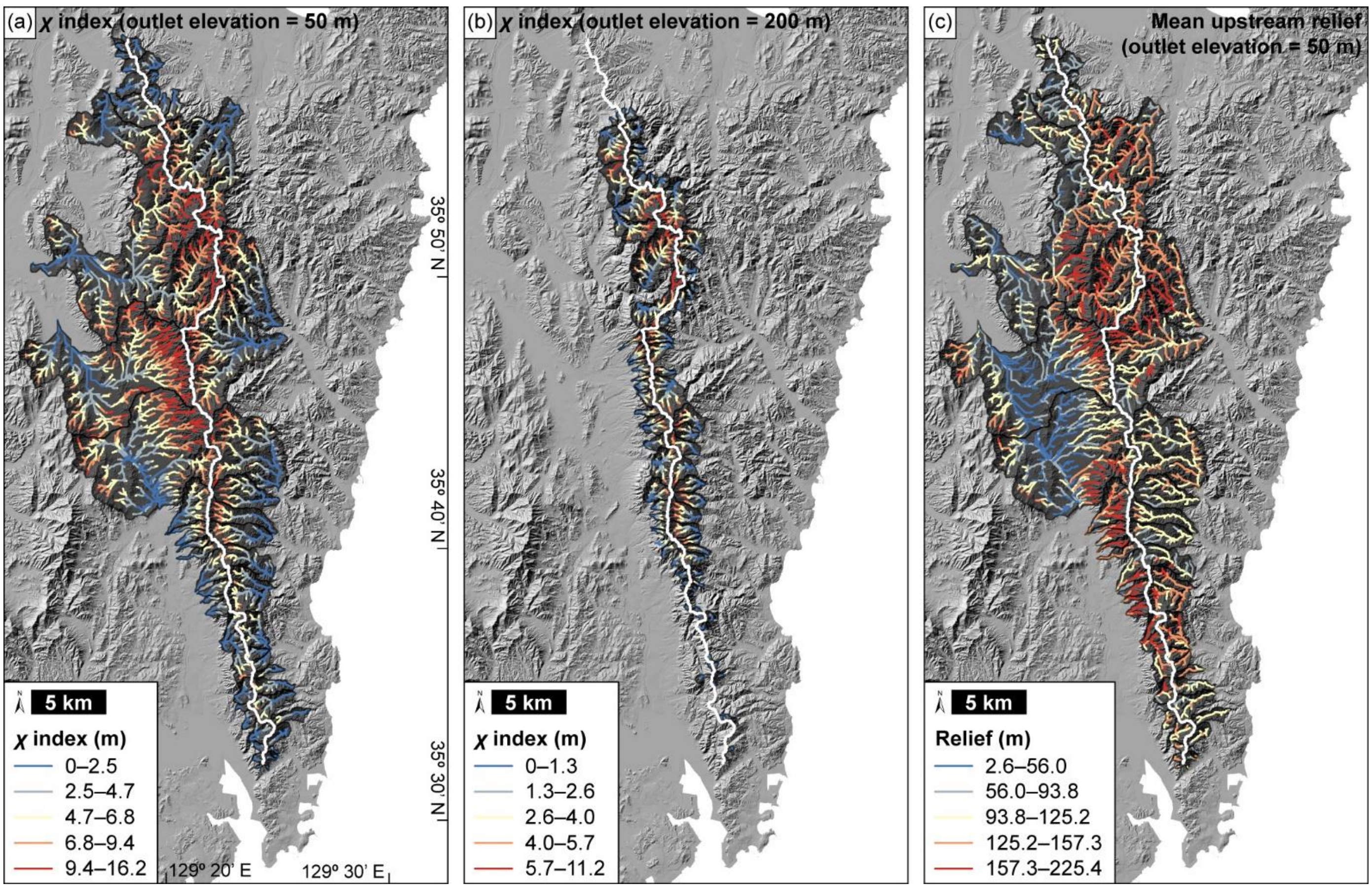

Figure 6: (a and b) Variations in χ index values analysed with base-level elevations of 50 and 200 m, respectively. A reference concavity index (θ_{ref}) value of 0.45 was applied, and the reference drainage area (A_0) was set to unity for calculation. χ index values at channel heads on the western flank are higher than those on the eastern flank in the northern part of the study area, whereas the χ indices on the eastern flank are higher than those on the western flank in the southern part of the study area. (c) Mean upstream relief calculated within a radius of 200 m. Relief values at channel heads are mostly higher on the western flank than those at the channel heads on the eastern flank.

We plotted our topographic analysis results (Fig. 6) to determine whether and if so, how the topographic metrics vary along and across the MDD (Fig. 7). The along-MDD variation in each topographic metric shows the relative highs and lows. The swath profile exhibits the highest peak around 42 km of the horizontal axis and relatively high peaks around 25, 51, and 60 km (Fig. 7a).

The western k_{sn} with a base-level elevation of 50 m shows the highest value 59–70 km ~~of~~ along the horizontal axis. The ~~one~~ segment with a base-level elevation of 200 m has the higher values around 43 and 59–70 km of the horizontal axis. The western mean upstream relief with a base-level elevation of 50 m exhibits the higher values around 65 and 72–80 km, and the one with a base-level elevation of 200 m has higher values at distances of around 43 and 63 km. Lastly, the western χ index with a base-level elevation of 50 m shows the highest peak around 41–50 km of the horizontal axis, and the one with a base-level elevation of 200 m has relatively small variation along the MDD but shows the higher values 32–42, 53, and 60 km of horizontal axis.

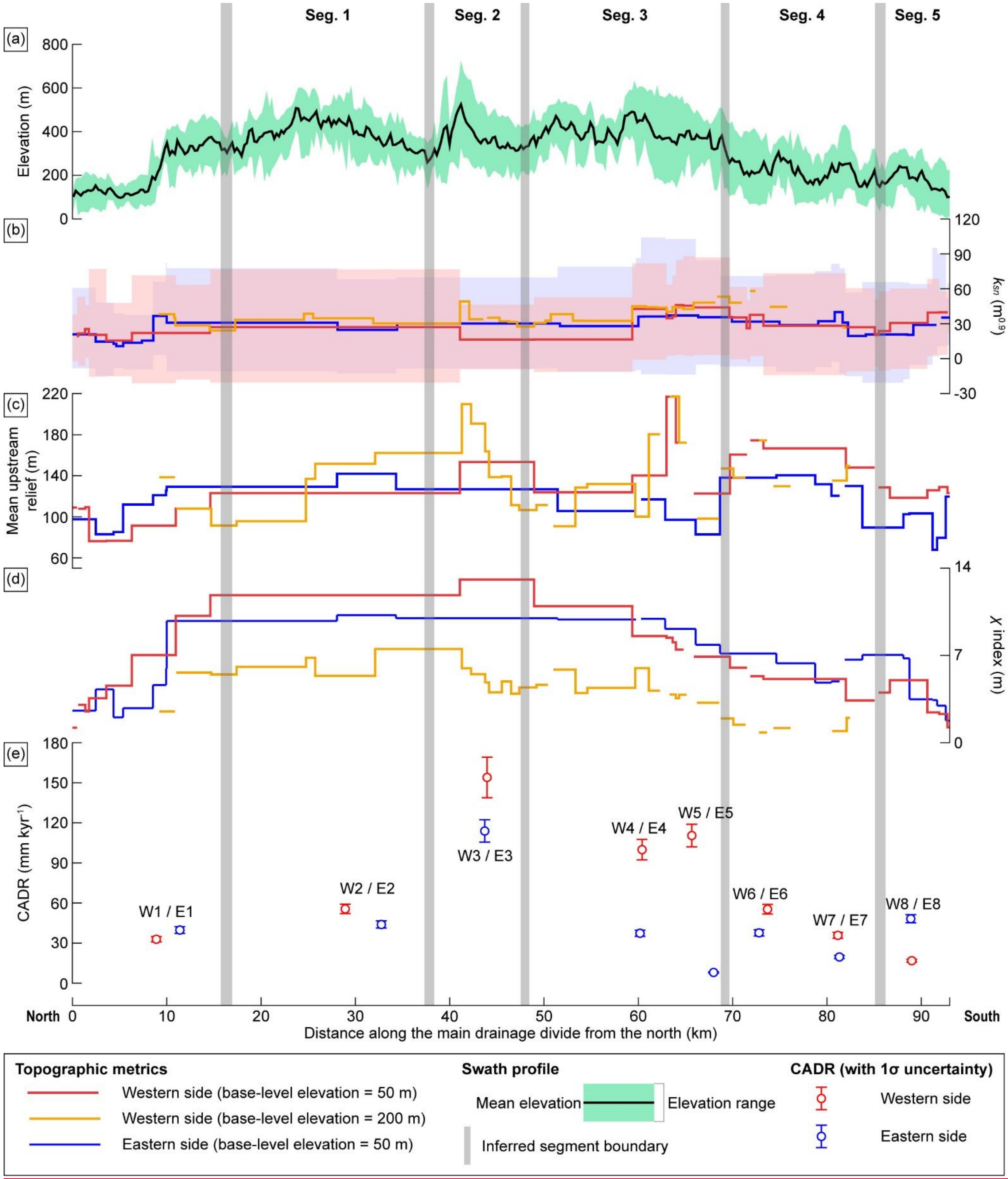

Seg. 1
Seg. 2
Seg. 3
Seg. 4
Seg. 5
(a)
Elevation (m)
(b)
k_{sn} ($m^{0.9}$)
(c)
Mean upstream relief (m)
(d)
χ index (m)
(e)
CADR (mm kyr⁻¹)
W1 / E1
W2 / E2
W3 / E3
W4 / E4
W5 / E5
W6 / E6
W7 / E7
W8 / E8
North
South
Distance along the main drainage divide from the north (km)
Topographic metrics
Western side (base-level elevation = 50 m)
Western side (base-level elevation = 200 m)
Eastern side (base-level elevation = 50 m)
Swath profile
Mean elevation
Elevation range
Inferred segment boundary
CADR (with 1σ uncertainty)
Western side
Eastern side

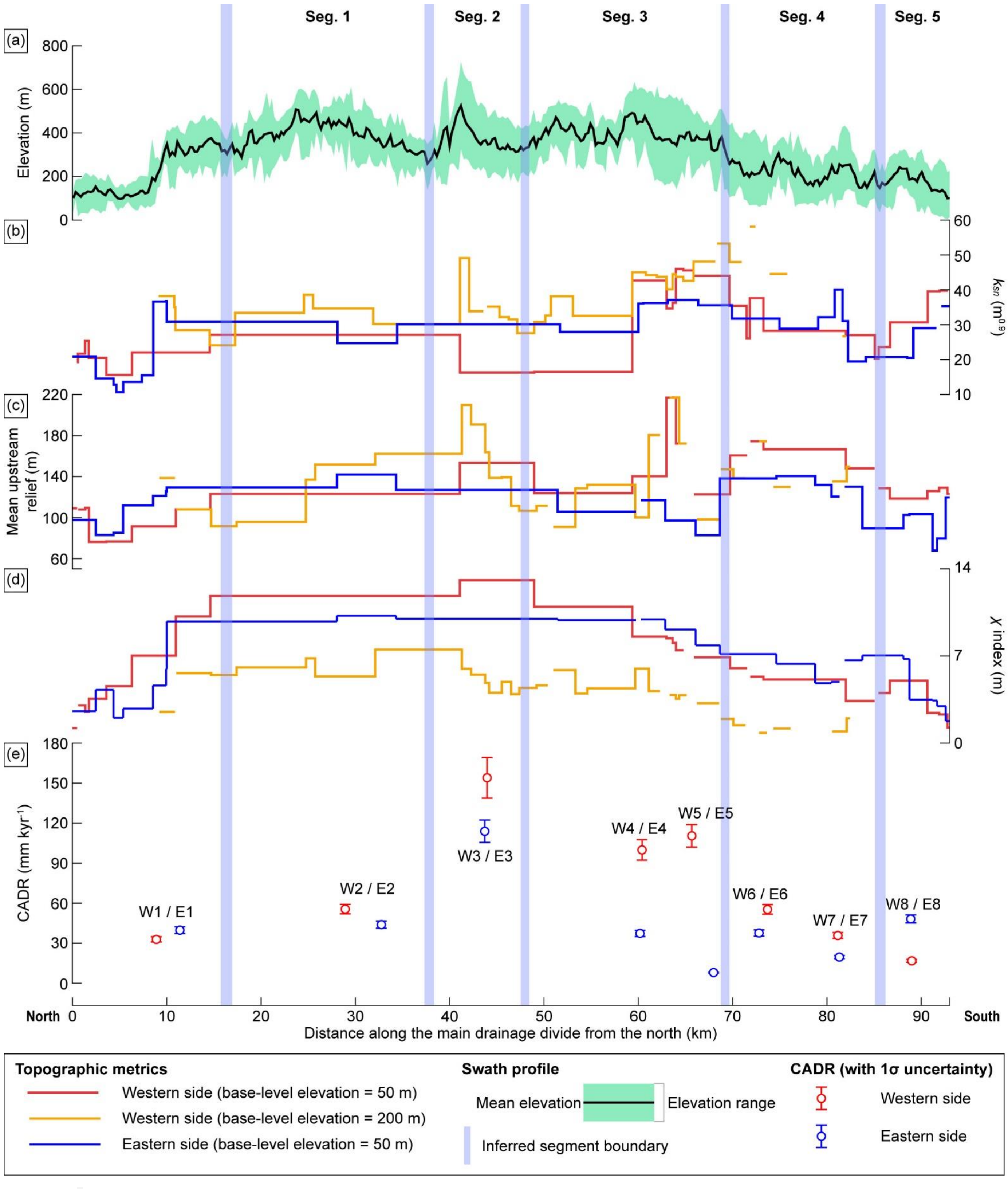

Figure 7: Variation in each topographic metrics along the MDD and fault segmentation proposed for the UFZ. (a) Swath profile along the MDD with an area width of 3 km centred on the MDD. The green-shaded area represents the minimum to maximum elevation. (b-d) Western topographic metrics extracted with a base-level elevation of 50 m is represented by a red solid line, those extracted with a base-level elevation of 200 m by an orange solid line, and eastern topographic metrics extracted with a base-level elevation of 50 m by a blue solid line. (b) Catchment-averaged k_{sn}. 1σ uncertainties of the k_{sn} values extracted with the base-level elevation of 50 m on the western and eastern flanks are marked with the red- and blue-shaded areas, respectively. (c) Mean upstream relief at channel heads. (d)

Mean χ index at channel heads. (e) Catchment-averaged denudation rate (CADR). Red and blue symbols represent the western and eastern) CADRs of each sample, along with their 1σ uncertainty.

There are some statistically significant differences in topographic metrics between those for the western and eastern flanks along the MDD (Fig. 7). The χ values are contrasted across 60 km: the western flank is 127 % higher than the eastern flank between 0–60 km, whereas the χ index values between the western and eastern flanks do not show a significant difference between 60–90 km (Fig. 7). Values of k_{sn} for the eastern-flank channels are up to 200 % higher than those for the western-flank channels within the 0–60 km section, whereas those for the western-flank channels are up to 137 % higher than those for the eastern-flank channels within the 60–90 km section (Fig. 7). We suggest that these differences arise from fault segmentation

4.2 In situ cosmogenic ^{10}Be

4.2.1 Variation in CADR within the study area

CADRs on the western flank range from 16.89 ± 1.00 to 155.23 ± 15.35 mm kyr^{-1}, and those on the eastern flank range from 7.35 ± 0.43 to 104.85 ± 7.71 mm kyr^{-1} (Table 2 and Fig. 3a). The integration times of these denudation rates cover the interval range of 4.5–95 kyr, during which the rates are implicitly assumed to have been steady. We plotted the CADRs in the along-MDD direction (Fig. 7e) and identified two main patterns, as follows. First, the CADRs on the western and eastern flanks are the highest near the central part of the MDD (W3: 155.23 ± 15.35 mm kyr^{-1} and E3: 104.85 ± 7.71 mm kyr^{-1}) and gradually decrease towards the northern and southern ends (Fig. 7e). The CADRs in the vicinity of a distance of 70 km from the north end of the MDD (the horizontal axis of Fig. 7), which were obtained using samples W5 and E6, are higher than those obtained from adjacent samples (W4 and W6; E5 and E7) (Figs. 3a and 7e). These higher CADRs, compared to their adjacent counterparts, contrast with the main spatial trend of decreasing CADR towards both ends of the MDD. However, these higher CADRs corresponds to the pattern of topographic metrics, such as mean upstream relief and k_{sn}, which also increase along this same trend (Fig. 7). Second, CADRs on the western flank are up to ~100 mm kyr^{-1} higher than those on the eastern flank. There is one exception at the southern end of the MDD (W8: 16.89 ± 1.00 mm kyr^{-1} and E8: 44.34 ± 2.81 mm kyr^{-1}), where the CADRs on the eastern flank are higher than those on the western flank (Figs. 3a and 7e).

Table 2: Catchment-averaged denudation rates calculated from cosmogenic *in situ* ^{10}Be measurement.

	Sample name	Latitude (° N, dd)	Longitude (° E, dd)	Elevation (m)	Production rate[a] Spallation (atoms g^{-1} yr^{-1})	Production rate[a] Muon (atoms g^{-1} yr^{-1})	^{10}Be conc.[b,c] (10^4 atoms g^{-1})	Denudation rate[c,d] (mm kyr^{-1})	Integration time[d] (kyr)
Western flank	W1	35.9409	129.3009	70	3.63	0.049	7.69 ± 0.15	32.94 ± 2.01	21.75
	W2	35.8230	129.3412	190	4.27	0.051	5.24 ± 0.13	55.94 ± 3.56	12.60
	W3	35.7825	129.3402	245	4.23	0.051	1.87 ± 0.15	155.23 ± 15.35	4.55
	W4	35.6964	129.3511	205	4.45	0.052	3.02 ± 0.15	100.56 ± 7.73	6.99
	W5	35.6634	129.3550	153	4.11	0.050	2.55 ± 0.13	111.27 ± 8.51	6.36
	W6	35.6284	129.3719	113	3.73	0.049	4.65 ± 0.15	55.90 ± 3.66	12.79
	W7	35.6026	129.3868	95	3.71	0.049	7.19 ± 0.16	35.95 ± 2.22	19.87
	W8	35.5506	129.3965	65	3.57	0.048	14.80 ± 0.20	16.89 ± 1.00	42.26
Eastern flank	E1	35.9188	129.3527	165	4.07	0.050	7.67 ± 0.20	36.65 ± 2.32	19.32
	E2	35.8213	129.3978	106	3.98	0.050	6.80 ± 0.14	40.52 ± 2.49	17.51
	E3	35.7923	129.3659	230	4.39	0.051	2.86 ± 0.13	104.85 ± 7.71	6.72
	E4	35.7062	129.3964	187	4.19	0.051	8.26 ± 0.17	34.91 ± 2.14	20.18
	E5	35.6612	129.3947	155	4.13	0.050	38.78 ± 0.45	7.35 ± 0.43	94.48
	E6	35.6400	129.3896	144	3.88	0.049	7.74 ± 0.15	34.72 ± 2.11	20.48
	E7	35.6021	129.4092	75	3.69	0.049	14.27 ± 0.21	18.02 ± 1.07	39.47
	E8	35.5670	129.4355	81	3.52	0.048	5.56 ± 0.15	44.34 ± 2.81	16.23

[a] Catchment-averaged production rate of *in situ* ^{10}Be was computed (Charreau et al., 2019), applying the LSDn scaling scheme (Lifton et al., 2014).

[b] Process blank ($4.37–4.53\times10^{-15}$; n = 6) was used for correction of background, and ratios of ^{10}Be/^{9}Be were normalized with 07KNSTD reference sample 5-1 ($2.71\times10^{-11} \pm 4.71\times10^{-13}$) of (Nishiizumi et al., 2007).

[c] Mean values and 1σ uncertainties are used.

[d] ^{10}Be half-life of 1.38×10^{6} yr (Chmeleff et al., 2010), density of the sample (ρ) of 2.7 g cm^{-3}, and attenuation length (Λ) of 160 g cm^{-2} (Braucher et al., 2011) were used for calculation of denudation rate and integration time.

4.2.2 Channel incision rates derived from ^{10}Be exposure ages of straths

We calculated channel incision rates using ^{10}Be exposure ages of bedrock straths and the present bedrock channel bed (Table 3). On the western flank, the exposure age of the present channel bed is 2.07 ± 0.12 kyr. The strath is 4.10 m higher than the channel bed, and two samples from the tread yield consistent ^{10}Be exposure ages of 5.11 ± 0.13 and 4.91 ± 0.13 kyr (mean: 5.01 ± 0.09 kyr) (Fig. 3). Dividing the height of the strath by the age difference between them {4100 mm / [(5.01 ± 0.09) − (2.07 ± 0.12)] kyr} yields a channel incision rate of 1394.56 ± 71.15 mm kyr^{-1}. On the eastern flank, the exposure age of the present channel bed is 12.30 ± 0.15 kyr, and the age of the strath, which is 2.73 m higher than the channel bed, is 24.98 ± 0.20 kyr. The calculated incision rate {2730 mm / [(24.98 ± 0.20) − (12.30 ± 0.12)] kyr)} is 215.30 ± 4.24 mm kyr^{-1}. Therefore, at the locations studied, the incision rate on the western flank is approximately 6.5 times higher than that on the eastern flank.

Table 3: Cosmogenic ^{10}Be surface exposure ages of bedrock strath terraces.

Sample name	Latitude (° N, dd)	Longitude (° E, dd)	Elevation (m)	Thickness (cm)	Topographic shielding	Quartz mass[a] (g)	Carrier mass (g)	^{10}Be/^{9}Be[b, c] (10^{-14})	^{10}Be conc.[c, d] (10^3 atoms g^{-1})	Exposure age[c, e] (kyr)
WT0-1	35.6985	129.3514	232	5.0	0.9098	21.277	0.438	1.35 ± 0.04	6.20 ± 0.36	2.07 ± 0.12
WT1-1	35.6985	129.3514	236	3.5	0.9968	20.620	0.413	2.15 ± 0.07	16.48 ± 0.40	5.11 ± 0.13
WT1-2	35.6985	129.3514	236	2.5	0.9968	20.328	0.387	2.17 ± 0.08	15.96 ± 0.41	4.91 ± 0.13
ET0-1	35.7069	129.3921	207	4.0	0.9478	20.036	0.371	4.22 ± 0.12	40.71 ± 0.48	12.30 ± 0.15
ET1-1	35.7069	129.3922	209	5.0	0.9518	20.171	0.440	7.16 ± 0.23	89.78 ± 0.73	24.98 ± 0.20

[a] Density of rock (ρ) of 2.7 g cm^{-3} was used.

[b] Ratios of ^{10}Be/^{9}Be were normalized with 07KNSTD reference sample 5-1 ($2.71\times10^{-11} \pm 4.71\times10^{-13}$) (Nishiizumi et al., 2007) and ^{10}Be half-life of 1.38×10^{6} yr (Chmeleff et al., 2010).

[c] Mean values and 1σ uncertainties are used.

[d] Process blank ($4.37–4.53\times10^{-15}$; n = 6) was used for correction of background.

[e] Ages are calculated assuming zero erosion via CRONUS-Earth online calculator (version 3.0) (Balco et al., 2008) with scaling factors, applying the LSDn scaling scheme (Lifton et al., 2014).

4.3 Landscape evolution modelling

The MDDs in the initial topographies of Cases A#, which simulated spatially uniform uplift during stage 1, are centrally located within the modelled domains (Figs. 8a and A1a). In both Cases A1 and A2, after stage 1, the χ indices at the channel heads on the western flank are comparable to those on the eastern flank (Figs. 10a and A1a). However, the MDDs in the initial topographies of Cases B#, which simulated a spatial gradient in uplift rate during stage 1, are biased towards the eastern flank of the modelled domain. After stage 1, the χ indices at the channel heads are lower on the eastern flank than on the western flank in both Cases B1 and B2 (Figs. 9a and A2a). The initial topographies of Cases A# and Cases B# exhibit differences in modelled positions of the MDDs and the patterns of χ indices. These differences are likely due to the variation in the spatial uniformity of uplift rate during stage 1 (uniform vs. non-uniform; Fig. 4b).

4.3.1 Cases A1 and A2

Cases A1 and A2 involved spatially uniform regional uplift during stage 1, followed by spatially variable local uplift related to faulting during stage 2. The modelling results for Cases A1 and A2 show similarities in drainage configuration (Figs. A1 and 8). During stage 2, the drainage patterns of the initial topographies in both cases undergo minimal change throughout the modelled domain. The MDDs in both cases remain virtually static, and the channels retain their original routes during stage 2 (Figs. A1a, A1b, 8a, and 8b). The spatial distribution of χ indices in both cases also shows negligible differences compared with the initial topography. In addition, the statistical patterns of topographic metrics for the resultant topographies at the end of stage 2 are almost identical in the two cases (Figs. A1c and 8c). In both cases, the western- and eastern-flank χ indices after stage 2 show no statistical difference (p-value > 0.05). However, this pattern is inconsistent with the spatial distribution of uplift rate during stage 2. The western flank would show lower χ indices and higher mean upstream relief compared with the eastern flank, as the model simulated a higher uplift rate on the western flank than the eastern flank during stage 2.

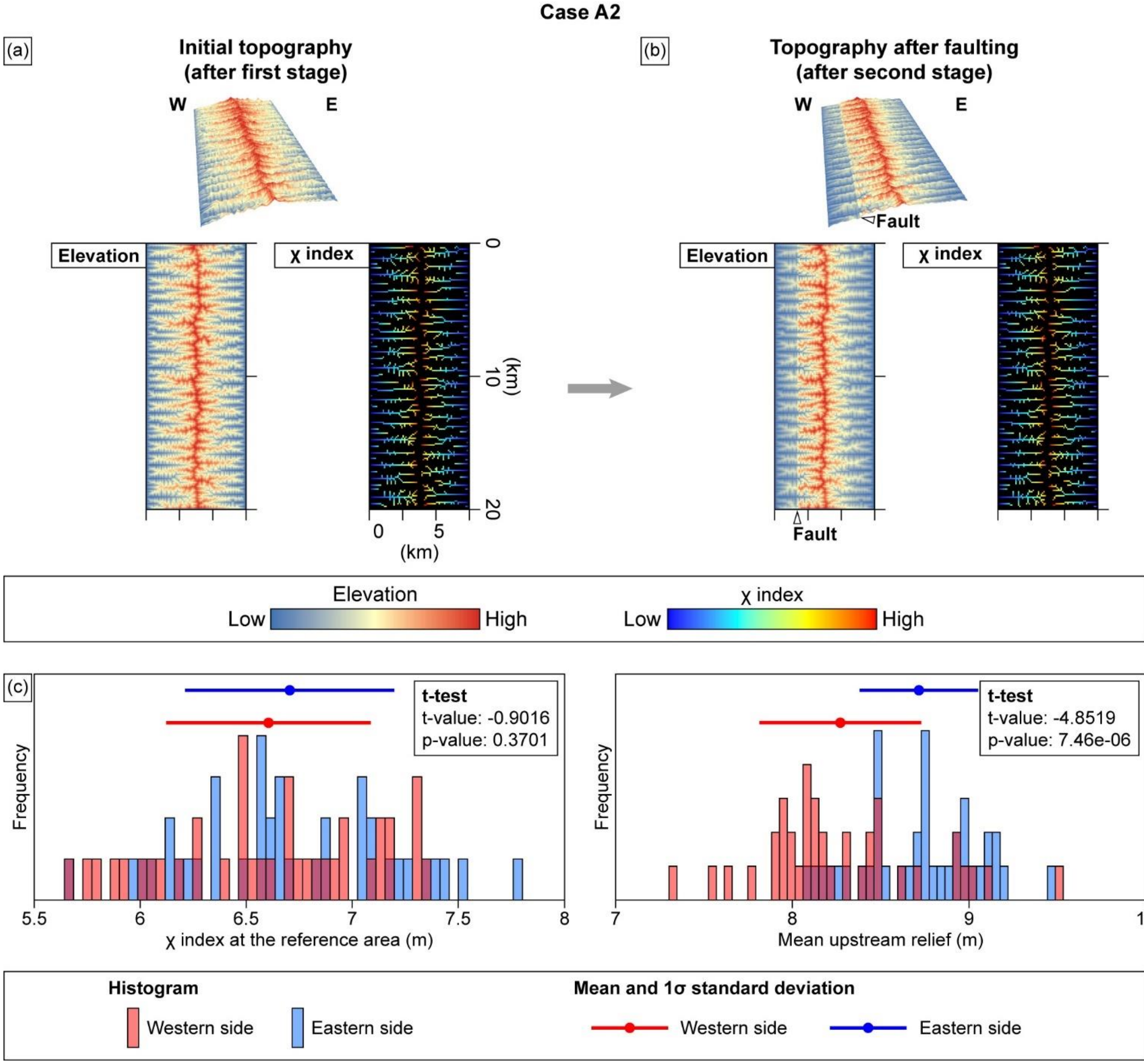

570 **Figure 8: Modelled landscape evolution for Case A2. (a) Inherited topography and χ index after stage 1, simulating a spatially uniform uplift rate of 80 mm kyr^{-1} over the modelled domain. (b) Topography and χ index after stage 2, simulating fault movement. (c) Histograms, mean values, and 1σ standard deviations for topographic metrics (χ index and mean upstream relief) at the channel heads on the western and eastern flanks of the MDD, extracted from the modelled topography at the end of stage 2.**

4.3.2 Cases B1 and B2

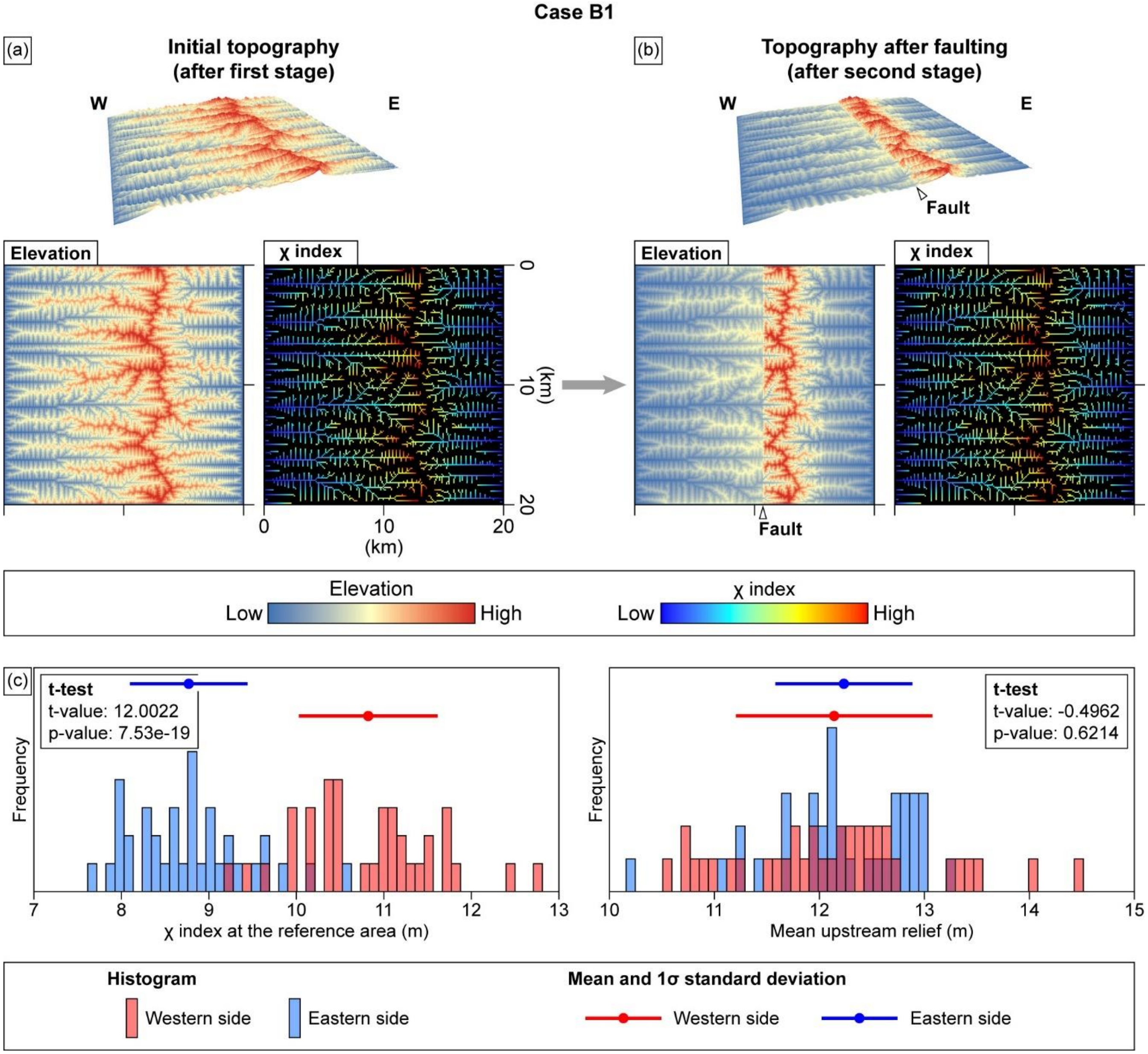

Figure 9: Modelled landscape evolution for Case B1. (a) Inherited topography and χ index after stage 1, simulating a spatially non-uniform uplift rate. The uplift rate is highest at the eastern boundary of the modelled domain (80 mm kyr^{-1}) and decreases with a spatial gradient of -2 mm kyr^{-1} km^{-1} towards the west so that the uplift rate is halved (40 mm kyr^{-1}) at the western boundary of the modelled domain. (b) Topography and χ index after stage 2, simulating the fault movement. (c) Histograms, mean values, and 1σ standard deviations for topographic metrics (χ index and mean upstream relief) at channel heads on the western and eastern flanks of the MDD, extracted from the modelled topography at the end of stage 2.

Cases B1 and B2 involved spatially variable regional uplift during stage 1, followed by spatially variable local uplift by faulting during stage 2. Case B1 also exhibits similar results to those for Case B2 (Figs. 9 and A2). The drainage patterns of these two cases however show noticeable changes during stage 2 when compared with Cases A#. During stage 2, the MDD migrates westwards by 100–800 and 100–1200 m in Cases B1 and B2, respectively (Figs 9a, 9b, A2a, and A2b). The heightened sensitivity of the MDD to uplift in Case B2 can be attributed to its shorter channels compared to those in Case B1, allowing the signal of fault activity to propagate more quickly from downstream to upstream. The western-flank channels in both cases shorten during stage 2, losing their upstream areas (Fig. 10b). In addition, the channels undergo subtle changes near the fault. For instance, some channels flowing from north to south or from south to north become shorter or disappear, whereas some new first- or second-order channels that are oriented transversely or obliquely to the fault develop in the vicinity of the fault (Fig. 10b). Despite these changes in drainage configuration during stage 2, the contrasting χ indices of the western- and eastern-flank channel heads observed in the initial topography persist through stage 2.

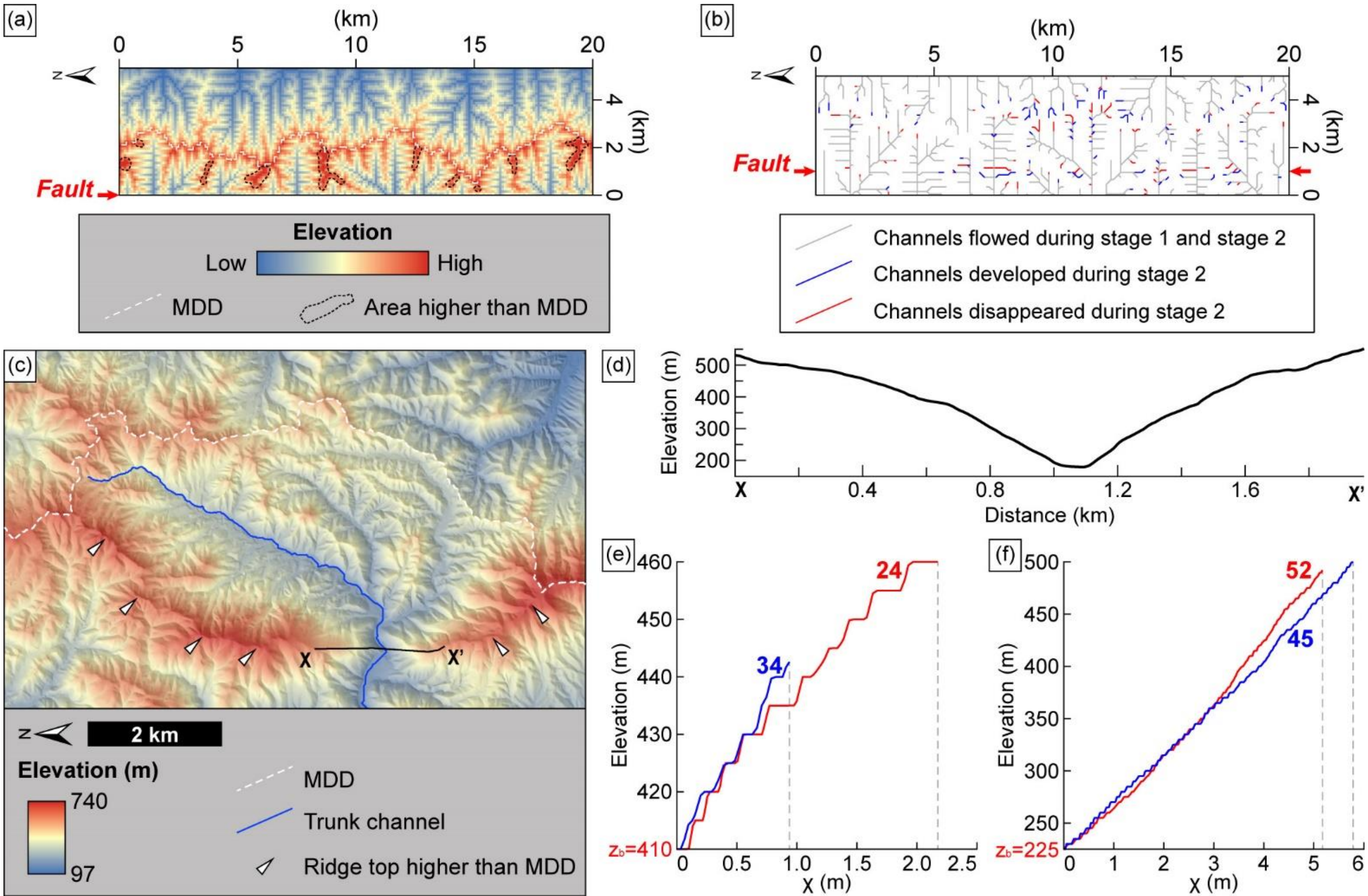

(a)
(km)
0 5 10 15 20
4 2 0 (km)
Fault
Elevation
Low High
MDD
Area higher than MDD
(b)
(km)
0 5 10 15 20
4 2 0 (km)
Fault
Channels flowed during stage 1 and stage 2
Channels developed during stage 2
Channels disappeared during stage 2
(c)
X X'
2 km
Elevation (m)
740
97
MDD
Trunk channel
Ridge top higher than MDD
(d)
Elevation (m)
500 400 300 200
X 0.4 0.8 1.2 1.6 X'
Distance (km)
(e)
460 450 440 430 420
Elevation (m)
34
24
z_b=410
0 0.5 1.0 1.5 2.0 2.5
χ (m)
(f)
500 450 400 350 300 250
Elevation (m)
52
45
z_b=225
0 1 2 3 4 5 6
χ (m)

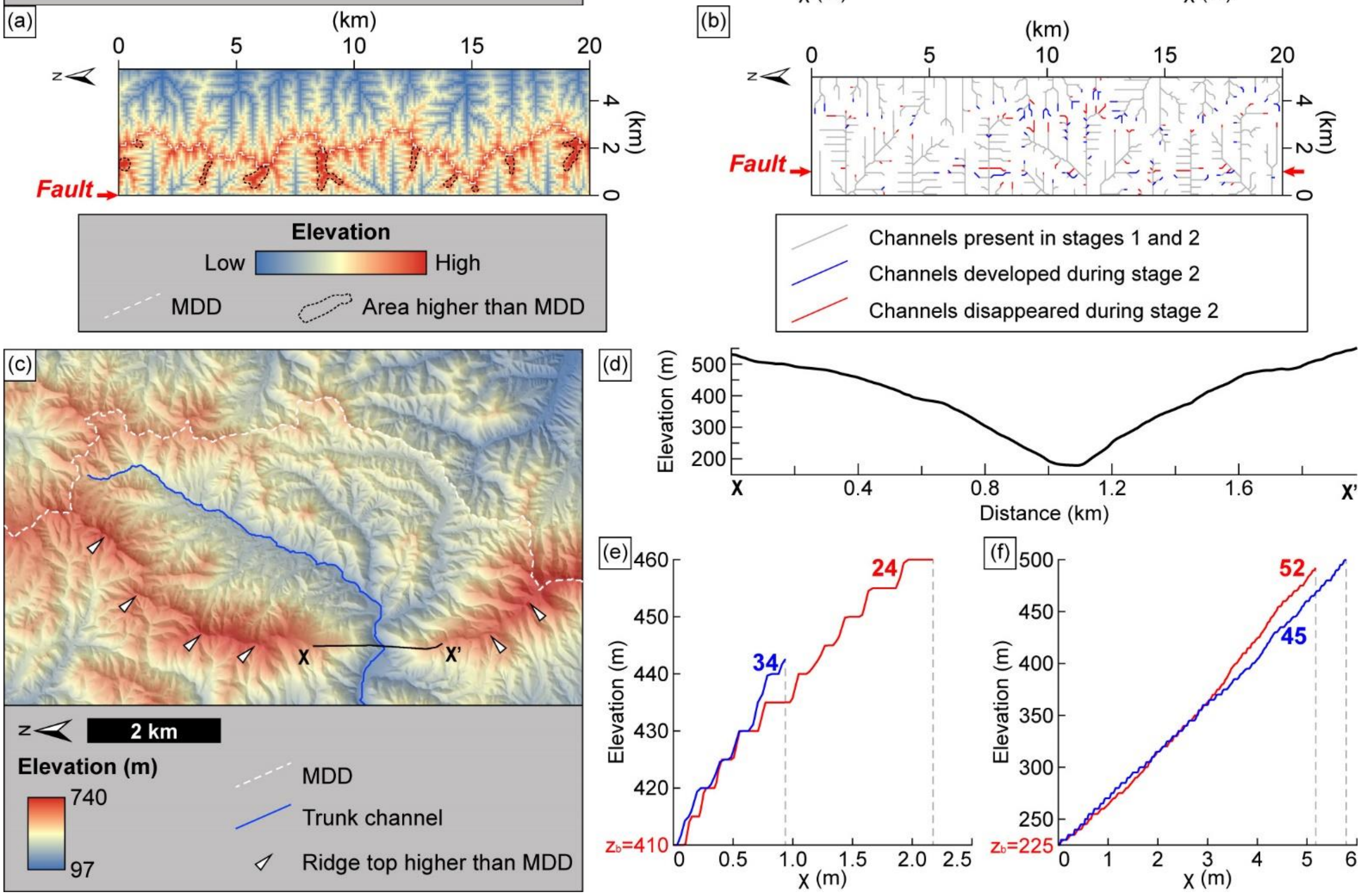

(a)
(km)
0 5 10 15 20
4 2 0 (km)
Fault
Elevation
Low High
MDD
Area higher than MDD
(b)
(km)
0 5 10 15 20
4 2 0 (km)
Fault
Channels present in stages 1 and 2
Channels developed during stage 2
Channels disappeared during stage 2
(c)
X X'
2 km
Elevation (m)
740
97
MDD
Trunk channel
Ridge top higher than MDD
(d)
Elevation (m)
500 400 300 200
X 0.4 0.8 1.2 1.6 X'
Distance (km)
(e)
460 450 440 430 420
Elevation (m)
34
24
z_b=410
0 0.5 1.0 1.5 2.0 2.5
χ (m)
(f)
500 450 400 350 300 250
Elevation (m)
52
45
z_b=225
0 1 2 3 4 5 6
χ (m)

Figure 10: (a) Resultant topography for Case B1, which simulates the northern part of the study area with asymmetric uplift (westward tilting). Areas with higher elevation than that of the MDD are observed and show similar features to the high ridge top within segment 1 (Fig. 10c). (b) Change in the routes of channels during stage 2 (faulting). The western-flank drainage system loses upstream area, whereas the eastern-flank drainage systems gain upstream area. Some channels parallel to the fault disappear, and new channels oriented oblique or transverse to the fault are developed. (c) The ridge top higher than the MDD in segment 1. The location of this figure is marked in Fig. 2a. This ridge has elevated owing to the higher uplift rate on the western flank since reactivation of the UFZ during the late Quaternary. The antecedent stream flowing within the upstream area in the vicinity of the MDD and the ridge has continued to erode this ridge. (d) Cross-profile of X–X' in Fig. 10c. The scale of the horizontal axis and vertical axis of this profile is 1:1. (e and f) χ-transformed profile of the uppermost reach of channels within segments 1 and 2, respectively. These channels are the same as those presented in Figs. 11a and 11c.

The topography of Case B1 after stage 2 exhibits similar patterns of topographic metrics to those of Case B2 (Figs. 9c and A2c). The eastern-flank χ indices are significantly lower than their western-flank counterparts (p-value < 0.05). In contrast, the eastern-flank mean upstream relief values are either comparable to (Case B1) or higher than (Case B2) those on the western flank. As with the results for Cases A#, Cases B# also display patterns of topographic metrics that differ from expectations. We expect the western flank to have lower χ indices than the eastern flank, in response to higher uplift rate on the western flank during stage 2.

5 Discussion

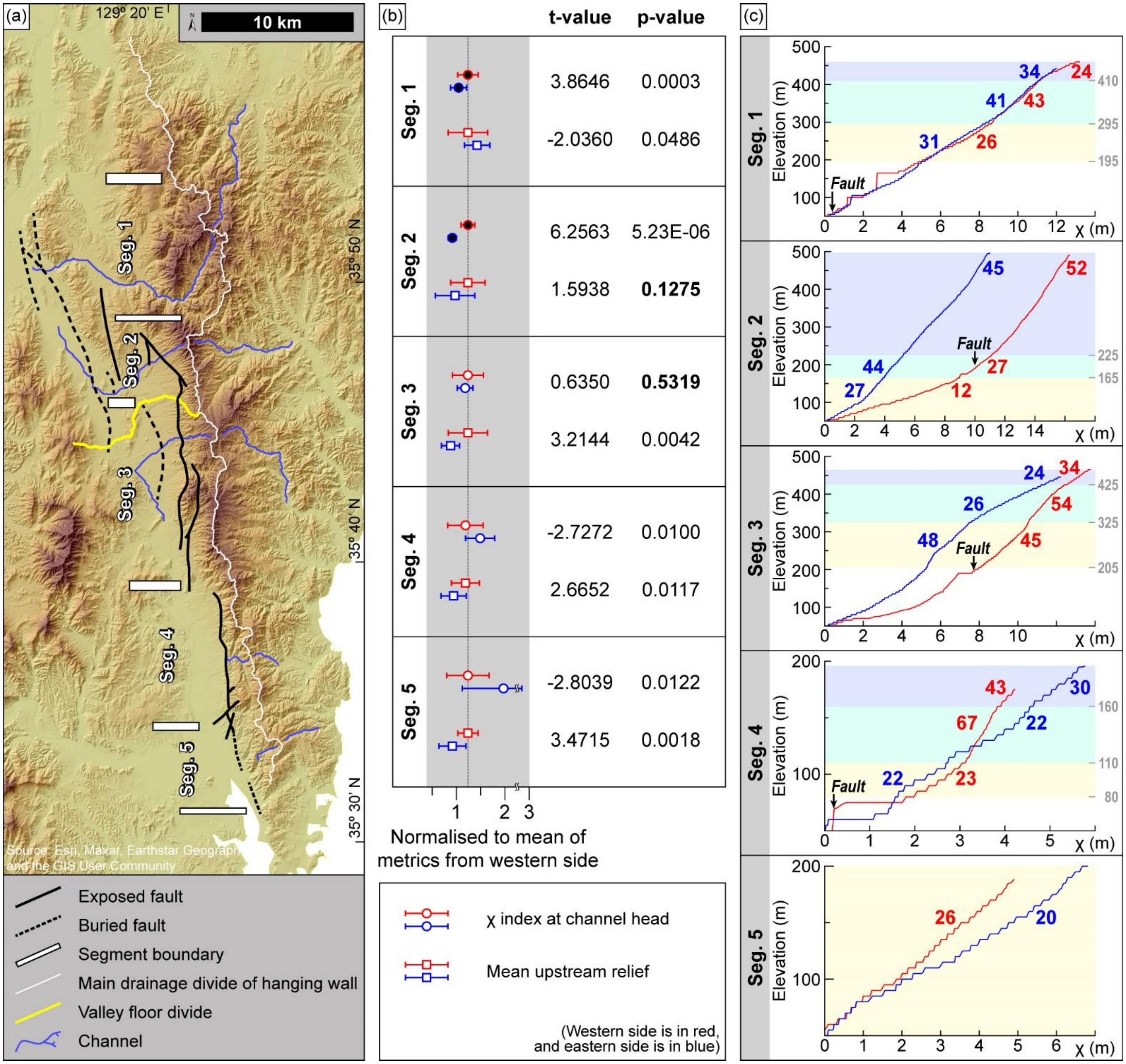

Figure 11: Our proposed segmentation of the UFZ, with values of topographic metrics analysed for each segment. (a) Segmentation of the UFZ proposed in this study. The locations of segment boundaries are the same as those marked in Fig. 7. The segment boundaries are marked with white bars, and the MDD of the TMR is marked with a solid white line. (b) Mean values and 1σ standard deviation of topographic metrics within each segment, normalised to the mean value of each index from the western flank. Topographic metrics on the western flank are in red, and those on the eastern flank are in blue. Symbols filled with black represent decoupled χ indices. We performed Student's t-tests to compare these metrics between the western and eastern flanks. P-values exceeding the threshold of 0.05 (statistical significance of 95 %) are given in bold, which indicate that the mean values of the western- and eastern-flank are not statistically significantly different. (c) χ-transformed profiles for one western-flank and one eastern-flank channel from each of the segments shown in Fig. 11a. The numbers represent ksn of each reach of channel. The profiles for channels on the western flank are plotted with a red line, and those on the eastern flank are plotted with a blue line.

5.1 Segmentation of the UFZ

Extensive faults or fault zones typically undergo repeated fault patch rupture along specific portions or segments of their lengths. Such faults are called segmented faults with each segment that ruptures during a single seismic event termed an 'earthquake segment' (McCalpin, 1996). Identification of fault segmentation is crucial for understanding the geometry, mechanism, and seismological behaviour of the neotectonic faults. However, defining the earthquake segment unequivocally can be challenging unless multiple historical ruptures have been preserved and can be observed, such as that observed in segmented normal fault arrays in low-strain arid settings (Moore and Schultz, 1999). Further, McCalpin (1996) distinguished five different types of fault segments: (1) rupture, (2) behavioural, (3) structural, (4) geological, and (5) geometric segments (table 9.7 of McCalpin, 1996). The definitions of these segments are listed in order from the most stringent to least restrictive, and the rupture segment is synonymous with the previously defined earthquake segment.

In this study, the UFZ was divided into five geological segments defined using geomorphic indicators (McCalpin, 1996) and considering fault geometry. Where segments are arranged across stepovers or bends, there may be a zone of cumulative vertical displacement deficit, which is termed a 'displacement trough', in the intersegment zone (Cartwright et al., 1995; Dawers, 1995; Manighetti et al., 2015). We identified displacement troughs of the UFZ with a relatively low tectonic activity on the basis of geomorphic evidence, such as lows in the swath profile, k_{sn}, relief, and χ index along the MDD (Fig. 7). We reason that relatively low tectonic activity correlates with low values in these topographic metrics, as suggested in earlier pioneering studies (Bull, 1977; Cox, 1994; Keller and Pinter, 1996). Areas along the MDD where the swath profile, k_{sn}, and relief values are relatively lower compared to other parts are interpreted as zones of lesser tectonic activity.

Accordingly, we divided the UFZ into five segments (segments 1–5; Figs. 7 and 11). The northern boundary of segment 1 is near the northern tip of the NNW–SSE-striking buried fault. There are lows in the swath profile, mean upstream k_{sn}, and relief extracted at the base-level elevation of 200 m (Fig. 7a and orange lines in Figs. 7b–7c). The intersegment zone between segments 1 and 2 is recognised by the low in the swath profile and the relatively low k_{sn} extracted at the base-level elevation of 200 m (Fig. 7a and orange line in Fig. 7b). The strike of an exposed fault along the mountain front also changes abruptly from NNW–SSE to NW–SE in this intersegment zone (Fig. 11a). Segment 2 has one of the highest swath profiles and high values of other topographic metrics, which also coincide with the highest observed CADR for the entire study area found in this segment (Fig. 7). We divided segment 2 from segment 3 at the point where the next set of lows in the swath profile, k_{sn} and relief appear (Fig. 7a and orange lines in Figs. 7b and 7c). The χ index also have relatively low values at this proposed segment transition~~there~~ (orange lines in Fig. 7d). Further, a NW–SE-striking fault trace terminates between segments 2 and 3, and the strike of the exposed fault changes to N–S. In addition, we found a valley floor divide in this intersegment 2–3 zone (Fig. 11a). We demarcated the boundary between segments 3 and 4 at a fault step (jog). The swath profile in this intersegment 3–4 zone shows a marked low (Fig. 7a), and relief is also low (both red and orange lines in Fig. 7c). The intersegment zone between segments 4 and 5 is characterised by lows in the swath profile and k_{sn} (Fig. 7a and red lines in Fig. 7b), and relatively low values for the other topographic metrics. The NNW–SSE-striking main fault strand is crosscut by NE–SW-striking minor faults, and additionally, an exposed fault terminates in this intersegment 4–5 zone.

The longest segment (Segment 3) is about 10.25 km long, and the shortest segment (Segment 2) is about 4.72 km long (Fig. 11a). Our proposed segment lengths are within the range of surface rupture lengths (SRLs) derived from empirical equations for reverse faults that describe the relationship between earthquake magnitude and SRL (Bonilla et al., 1984; Wells and Coppersmith, 1994). For example~~Accordingly~~, assuming a possible maximum earthquake magnitude of M_W 7.0 (Slemmons and Depolo, 1986; Kyung, 2010), the maximum SRL could be 25.60 km (Bonilla et al., 1984) or 43.58 km (Wells and Coppersmith, 1994). If the SRL is calculated using the magnitude of the Pohang earthquake (M_W 5.4; Fig. 1a), the predicted SRL would be 0.46 km (Bonilla et al.,

1984) or 2.13 km (Wells and Coppersmith, 1994). Given these calculations, our proposed geomorphic segmentation lengths seem reasonable, and our proposed segments appear to be physically realistic.

A recent study (Cheon et al., 2023) also divided the incised valley containing the UFZ on the basis of: (1) differences in fault-hosting rocks, and (2) width of the deformation zone. These authors segmented the UFZ into only two parts, with the division occurring between what we identify as segments 3 and 4 in the current study. We attribute this difference to the different segmentation criteria used and argue that our geomorphic-based fault segmentation has several advantages. First, the use of topographic metrics allows an indirect assessment to be made of the relative tectonic activity ~~over wide study areas~~ with spatial continuity over wide study areas. Fault outcrop studies and trench surveys do not have spatial continuity because they provide only point-specific information. Although determining fault segmentation based on observed slip rates would be most accurate, it is impractical due to the large number of geological surveys that would be required to obtain spatially continuous results. Second, geomorphic evidence can be used effectively even in areas where surface deformation is only weakly exposed. It is difficult to identify direct surface deformation from faulting in Korea because of the low slip rates, rapid physical and chemical erosion, and dense vegetation. However, topography and geomorphology can provide meaningful information on tectonic activity, as the present topography and geomorphology ~~is~~are a cumulative result of all past processes.

5.2 Geomorphic evolution of the eastern block of the UFZ in response to tectonic movement

We next used the similarities in the patterns of topographic metrics for each fault segment and the modelled topographies to interpret the geomorphic evolution of the eastern block of the UFZ (Figs. 8, 9, 11, A1c, and A2c). The χ index is suitable for indicating potential future divide mobility, while cross-divide differences in mean upstream relief are better suited to evaluate short-term divide mobility (Forte and Whipple, 2018; Zhou et al., 2022). Although we employed realistic settings for all boundary conditions in the models, based on a comprehensive understanding of the tectonic, geological, and geomorphic processes in the study area, it is acknowledged that there are likely to be discrepancies between the modelled and actual settings of variables (e.g., coefficient of erosion, uplift rate, and its spatial gradient) and epistemic uncertainties.

Since the topography along the MDD varies significantly, each metric (e.g., mean upstream relief or χ index) will encompass a broad spectrum of values. Comparing these means and standard deviations from the western and eastern flanks across the entire MDD might mask any genuine differences between the flanks, leading to a ‘Type II error (false negative: failing to detect a real difference)’. Therefore, we compared each topographic metric from the western and eastern flanks, segment by segment.

For segments 2–5, all topographic metrics, except for χ index, generally show a coupled pattern (higher western-flank mean upstream relief and CADR), which indicates higher erosion rates on the western flank (Fig. 9b). In contrast with mean upstream relief and CADRs, the χ anomaly between western and eastern flanks for each segment is inconsistent. The western-flank χ indices in segments 1 and 2 are higher than those of the eastern flank (p-value < 0.05), the same as those of the eastern flank in segment 3 (p-value > 0.05), and lower than those of the eastern flank in segments 4 and 5 (p-value < 0.05). This inconsistency of χ anomaly throughout the study area is related to its decoupling from the CADR, channel incision rate, and mean upstream relief in segments 1 and 2. The χ indices in segment 1 are decoupled from the higher CADR and incision rate on the western flank, and those in segment 2 are decoupled from not only CADR and incision rate but also the mean upstream relief. These decoupled χ indices in segments 1 and 2 (i.e., lower χ indices on the eastern flank of TMR) contradict what would be generally expected from the higher CADRs, channel incision rates, and mean upstream relief on the western flank compared with the eastern flank.

To clarify our landscape evolution modelling approach, we grouped the five proposed geomorphic segments into two distinct sections corresponding to the northern and southern parts of the UFZ, following but modifying the work of Cheon et al., (2023) as follows. Our ~~. The~~ northern part comprises segments 1 and 2, and the southern part contains segments 3, 4, and 5. Delineation of the boundary between the northern and southern parts was based on the following criteria: (1) the E–W width of the eastern block of the UFZ at the centre of segment 3 is half that of segment 1, (2) the pattern of χ indices shows a noticeable difference at the boundary between the northern and southern parts (i.e., decoupled versus coupled χ indices), (3) the valley floor divide may be a natural boundary between the two parts, and (4) there is an abrupt change in the orientation of faults across this boundary from NNW–SSE to N–S.

5.2.1 Northern part of the UFZ: segments 1 and 2

The geomorphic evolution of the northern part of the UFZ, which is characterised by lower χ indices on its eastern flank, is better explained by Case B1 than Case A1 (Figs. 9c and 11b). χ indices differ markedly between Cases A1 and B1, but the only difference in boundary conditions between these two models is the spatial uniformity of uplift during stage 1. Case A1 involves spatially uniform uplift, and Case B1 involves spatially variable uplift during stage 1 (Fig. 4). We interpret the lower χ indices on the eastern flank of segments 1 and 2, in comparison to the western flank, as a result of the influence of inherited topography. The northern part of study area may have been in topographic and geometric disequilibrium (i.e., biased MDD eastwards and asymmetric χ indices). This disequilibrium is caused by the asymmetric uplift during stage 1 and has persisted to the present day, as it is simulated in Case B1 (Fig. 9). Topographic and geometric disequilibrium and its persistence by the asymmetric uplift have also been identified in other modelled cases and natural systems (Willett et al., 2014; Forte and Whipple, 2018; Zhou et al., 2022; Zhou and Tan, 2023). In such cases, disequilibrium caused by the asymmetric uplift persists even after the onset of spatially uniform uplift, until the area reaches equilibrium and steady state through adjustment to the uniform uplift (Willett et al., 2014; Forte and Whipple, 2018). In the present study, the northern part of the UFZ has likely remained in disequilibrium as a result of the asymmetric uplift prior to Quaternary faulting and is still in transient state to attain equilibrium even after stage 2.

Within the northern part of the study area, segments 1 and 2 also show distinct patterns in mean upstream relief (Fig. 11). The differences between the two segments can be attributed to two possible factors: (1) the channel length between the fault and the channel head and (2) tectonic activity. Channel lengths between the fault and the channel heads are longer in segment 1 than in segment 2. In segment 1, buried faults are developed in the incised valley, far to the west from the mountain front (Cheon et al., 2023). The response time of a channel to tectonic events increases with increasing channel length between the fault and channel head. Therefore, in segment 1, it is plausible that the most recent tectonic signal from Quaternary fault slip has not yet been transferred to the channel head. Secondly, the inferred tectonic activity, based on topographic metrics and the CADR (Fig. 7), is higher in segment 2 than that in segment 1. Topographic metrics might be expected to have responded less sensitively to uplift in segment 1 because of its lower tectonic activity than that of segment 2.

5.2.2 Southern part of the UFZ: segments 3, 4, and 5

The pattern of measured χ indices in the southern part of the UFZ is similar to that of Case A2 (Figs. 8c and 11b). Unlike the northern part of the UFZ, the modelled outcome of Case A2 implies that the southern part of the UFZ had achieved topographic and geometric equilibrium before stage 2 (Fig. 8a). The lower western-flank χ indices as compared with those for the eastern flank may indicate the adjustment of channels to a higher uplift and erosion rates on the western flank after Quaternary reverse faulting of the UFZ. This rapid adjustment to the tectonic perturbation may result from the shorter channel length (between the fault and the channel head) in segments 3–5 compared with the northern part of the UFZ. The western-flank χ indices in segments 4 and 5 are lower than the corresponding eastern-flank values. However, there is no difference in χ index values between the western and eastern flanks in segment 3, which can be attributed to the low base-level elevation (z_b) set to calculate the χ index (50 m a.s.l.). This low base-level elevation resulted in the integration of a much further downstream reach than the fault location in segment 3, which is less relevant to tectonic uplift (Fig. 11a and 11c). The upper reaches of the fault have higher k_{sn} values on the western than the eastern flank, consistent with the pattern of values of the other topographic metrics, CADR, and channel incision rate.

We next used χ indices from the modelled topography and those observed in the study area to establish the geomorphic evolution of the eastern block of the UFZ. The northern part of the block underwent spatially variable uplift prior to Quaternary reverse faulting on the UFZ, resulting in the observed asymmetric topography. Conversely, the southern part of the block underwent spatially uniform uplift, attaining topographic and geometric equilibrium prior to Quaternary reverse faulting. Our interpretation on the geomorphic evolution of the eastern block of the UFZ is based on a generalised concept of the influence of pre-existing topography on subsequent geomorphic processes. The pre-existing topography, referred to as 'inherited topography', denotes the topography that existed prior to the event of interest. This inherited topography may include, for example, the channel length governed by the shape of the block and the degree of asymmetry of the topography controlled by the orientations of geological features (e.g., faults) and previous tectonic movements. The four modelling cases in this study simulated different inherited topographies but the same tectonic movement. Our model results demonstrate that the geomorphic response to subsequent tectonic movement is influenced by the inherited topography and that topographic metrics (such as the χ index) can be used to measure this influence.

5.3 Migration of the MDD and landscape evolution

Previous assessments of divide mobility have relied on comparing topographic metrics, such as the χ index and Gilbert metrics, of opposing sides of MDD (Gilbert, 1877; Willett et al., 2014; Forte and Whipple, 2018; Kim et al., 2020; Zeng and Tan, 2023). Understanding divide mobility is crucial to the investigation of landscape evolution, as it is a dynamic indicator of how the landscape evolves and may help determine the driving forces (i.e., tectonic movement and spatial patterns of uplift and erosion) of this evolution. However, we discovered in this study that the χ anomaly may not accurately reflect divide mobility in the UFZ study area because of the assumptions involved with determining~~of~~ χ index values. χ index can correctly indicate the divide mobility only when the area of interest has spatially uniform uplift, climate, lithology, and erodibility (Perron and Royden, 2013; Willett et al., 2014; Forte and Whipple, 2018). The χ-transformed profiles of channels with low base-level elevation (z_b = 50 m a.s.l.) in segments 2 and 3 show that the uppermost reaches of western-flank channels exhibit higher k_{sn} and χ index values than the eastern flank (Fig. 11c), giving contradictory interpretations on divide mobility. The higher k_{sn} on the western flank indicates eastwards divide migration, whereas the higher χ index on the western flank indicates westward divide migration. In this case, instantaneous divide mobility can be accurately evaluated only by comparing the uppermost reaches of channels from opposing sides of the MDD (Zhou et al., 2022). We adopted this approach for the northern part of the UFZ (segments 1 and 2), as the χ indices are decoupled from the CADR and bedrock incision rate there, as well being decoupled from additional topographic metrics used in this study (Figs. 10e, 10f, and 11b).

Uppermost reaches on the western flank in segment 1 exhibit lower k_{sn} and higher χ index values when compared to those from the corresponding eastern flank (Figs. 10c and 10e). This suggests that the MDD is migrating westwards in this segment, and that it is approaching topographic and geometric equilibrium (see **section 5.2.1**). Interestingly, we observed that the ridge top of an internal sub-basin on the western flank of the MDD in segment 1 is up to 380 m higher than the MDD itself (Fig. 10c). We propose two possible explanations for this high ridge top: (1) discrete stream capture of western-flank channels owing to the high uplift rate on the western flank; and (2) erosion of the ridge top by westward-flowing antecedent streams. The strongest evidence supporting stream capture is the presence of an elbow of capture, wind gap, gorge-like valley, and lower χ index at the channel head of a captor stream (Bishop, 1995; Willett et al., 2014). However, we could not identify any convincing evidence for stream capture, such as an elbow of capture or a gorge-like valley near the ridge top or wind gap near the MDD in segment 1, either in the field or on the DEM. The lower k_{sn} and higher χ index values of the western-flank uppermost reach in this segment also do not imply an aerial gain of the western-flank drainage system owing to stream capture (Fig. 10e). Furthermore, modelling results for Case B1 show similar features of high ridge tops without discrete stream capture. The resultant topography of Case B1, which simulates the landscape evolution of the northern part of the UFZ and spatially variable (asymmetric) uplift prior to late Quaternary faulting, shows some areas with higher elevations than that of the MDD (Fig. 10a). Therefore, we interpret that the streams flowing within the internal sub-basin surrounded by the MDD and the elevated ridge on the western flank (Fig. 10c) are the antecedent streams, flowing east to west. The high elevation of the ridge on the western flank of the MDD is ascribed to the higher uplift rate since Quaternary reverse faulting of the UFZ. The channels are hypothesised to have been subject to a sufficiently high erosion rate to retain the original stream route of the inherited topography in response to the higher uplift rate on the western flank, but this erosion rate was accordingly insufficiently high to capture parts of the drainage system on the eastern flank.

The western-flank uppermost reach in segment 2 has higher k_{sn} and lower χ index values than those on the eastern flank, as seen in the χ-transformed profile (Fig. 10f), whereas the profile with lower base-level displays a higher χ index on the western flank (Fig. 11c). χ indices at the channel heads are sensitive to base-level variations (Forte and Whipple, 2018). In the present case, the lower χ and higher k_{sn} values of the western-flank uppermost reach indicate short-term migration of the MDD towards the east. This inferred divide mobility is consistent with the results of other topographic metrics ~~providing a short-term view of topographic evolution,~~ such as elevation, mean upstream relief, and mean upstream gradient at the channel head, providing a short-term view of topographic evolution,. Consequently, we interpret that the MDD within segment 2 is migrating eastwards, just as is the MDD within segments 3–5, in which patterns of all topographic metrics are consistent with the eastward migration of the MDD.

6 Conclusions

The Ulsan Fault Zone (UFZ) has been one of the most active fault zones on the Korean Peninsula since its reactivation ~ 5 Ma. Our study area, the eastern, mountainous, hanging wall block of the UFZ, has undergone regional uplift under an ENE–WSW-oriented neotectonic maximum horizontal stress from 5 Ma to the present (i.e., neotectonics).~~after 5 Ma.~~ This study aimed to evaluate the relative tectonic activity along the UFZ, characterise the past and present geomorphic processes operating along the UFZ, and infer landscape evolution patterns in response to tectonic perturbation involving reactivation of the UFZ.

We evaluated the relative tectonic activity along the fault zone using topographic metrics, and catchment-averaged denudation rates (CADRs), and bedrock incision rates derived using *in situ* cosmogenic ^{10}Be. We proposed that ~~segmented~~ the UFZ is segmented into five ~~geological~~geomorphological zones based on the relative tectonic activity that we assessed. This study represents the first determination of UFZ segmentation based on relative tectonic activity inferred from topographic metrics and, more generally, presents a new method for determining fault segmentation in low-strain, temperate-humid settings.~~segmentation result based on the relative tectonic activity of the UFZ inferred from topographic metrics.~~

We also interpreted the tectono-geomorphic evolution of the study area by modelling landscape evolution and comparing the values and patterns of topographic metrics of the modelled topography with those observed in the study area. We interpret that the northern UFZ (segments 1 and 2) underwent regional asymmetric uplift (westward tilting) prior to Quaternary reverse faulting since ~ 2 Ma. The southern UFZ (segments 3–5) was negligibly affected by asymmetric uplift before Quaternary reverse faulting, as channel lengths (distance between the Ulsan Fault and the channel head) were sufficiently short to adjust quickly to the uplift. Our analysis and interpretation of the tectono-geomorphic evolution of the UFZ show that inherited topography can influence the subsequent geomorphic processes and topographic response to neotectonic reverse fault slip. The topographic metrics we utilized can therefore be regarded as characterising not only the present topography, but also as holding information resulting from the accumulation of a history of tectonic and erosion.

Our study clearly demonstrates that topographic metrics can effectively infer differential tectonic activity such as variable fault slip and surface uplift. Furthermore, modelling offers valuable insights into the potential influences of inherited topography in intraplate regions with extremely low strain rates and fault slip rates, coupled with high erosion rates.

Appendices

Appendix A. Results of landscape evolution modelling.

Appendix A contains landscape evolution modelling results for the two cases (Cases A1 and B2) that show dissimilar patterns of values of topographic metrics with northern and southern parts of the UFZ.

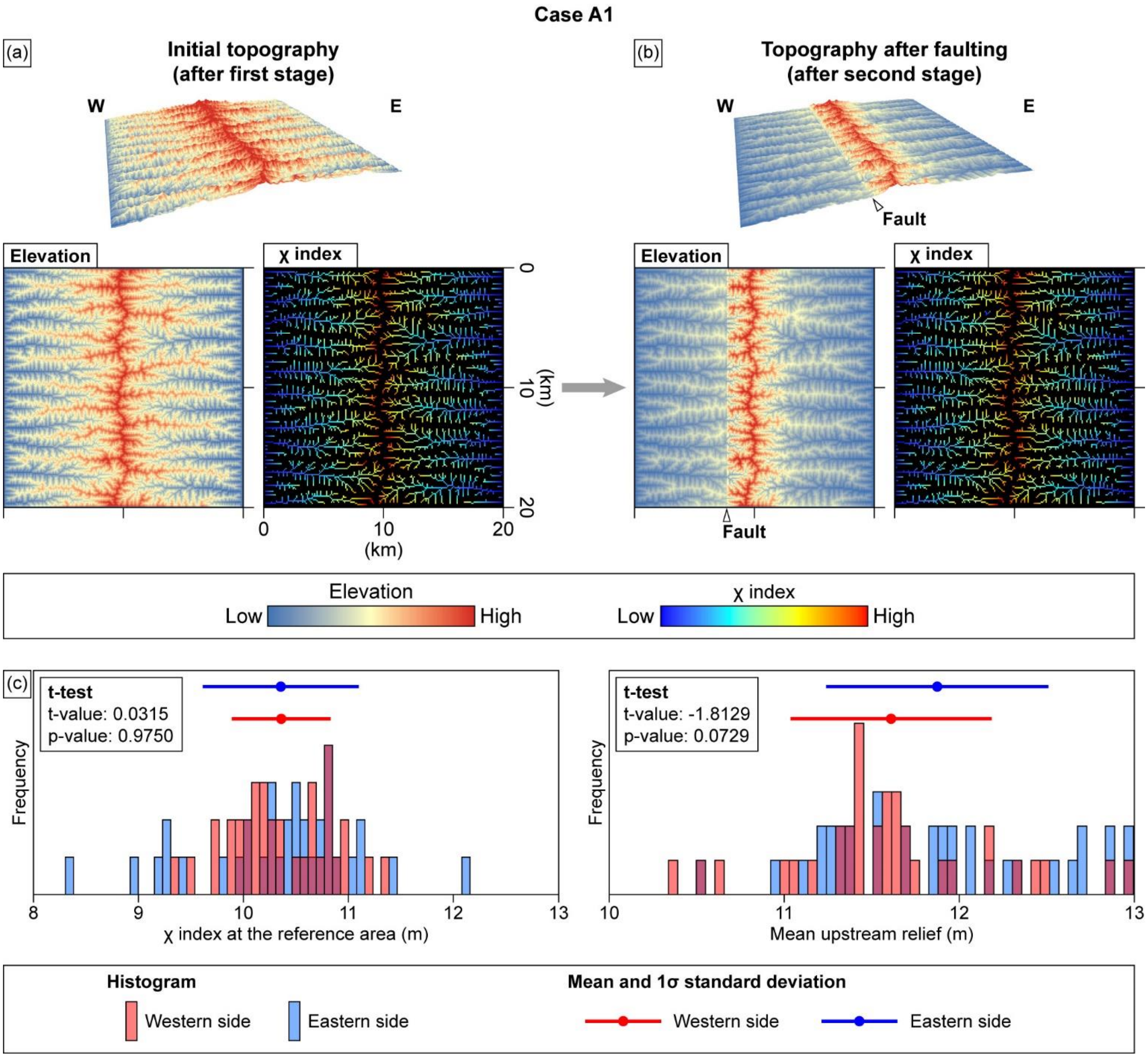

Figure A1: Modelled landscape evolution for Case A1. (a) Inherited topography and χ index after stage 1, simulating a spatially uniform uplift of 80 mm kyr^{-1} over the modelled domain. (b) Topography and χ index after stage 2, simulating fault movement. (c) Histograms, mean values, and 1σ standard deviations for topographic metrics (χ index and mean upstream relief) at the channel heads on the western and eastern flanks of the MDD, extracted from the modelled topography at the end of stage 2.

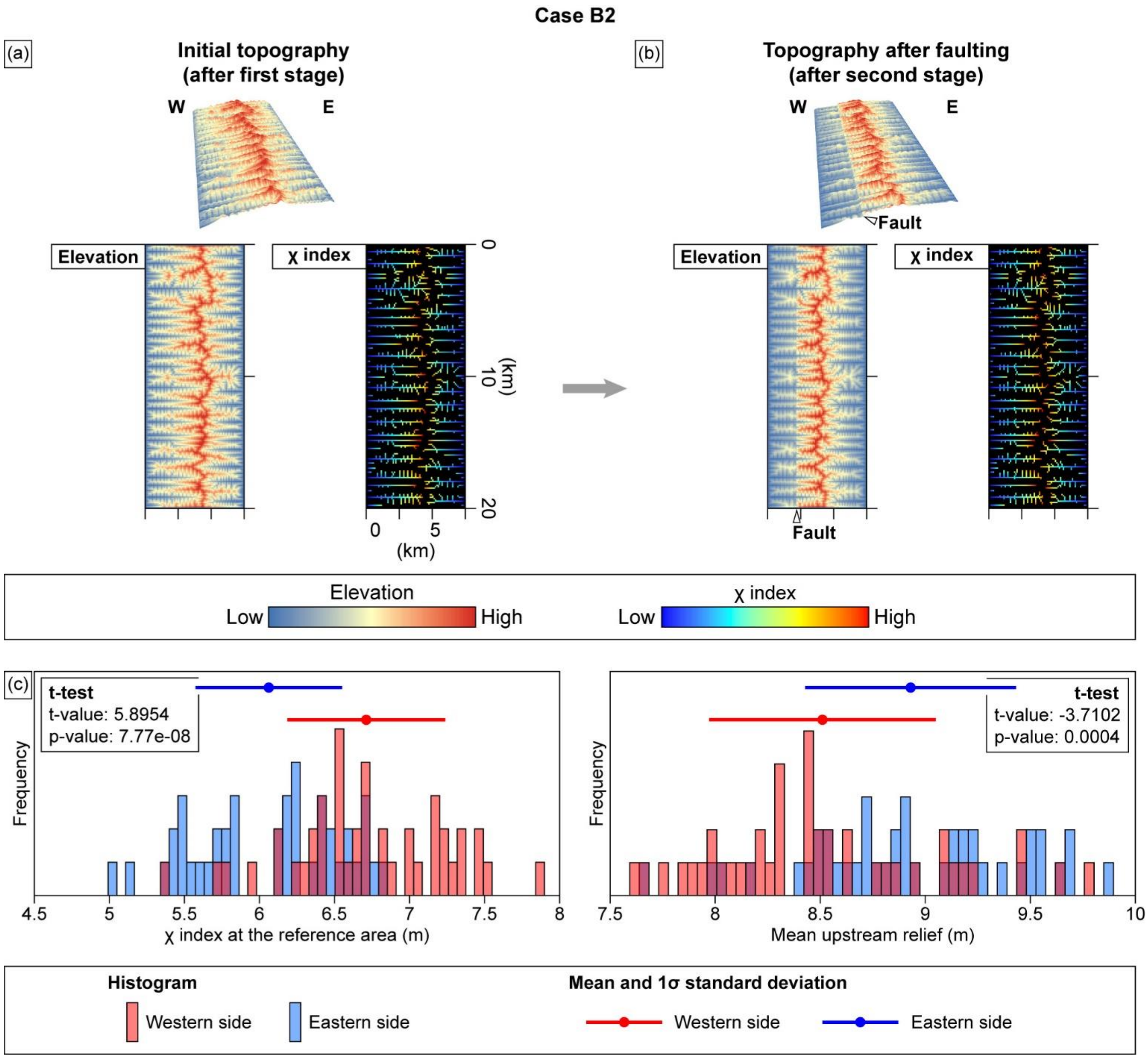

Figure A2: Modelled landscape evolution for Case B2. (a) Inherited topography and χ index after stage 1, simulating a spatially non-uniform uplift. The uplift rate is highest at the eastern boundary of the modelled domain (80 mm kyr^{-1}) and decreases with a spatial gradient of -2 mm kyr^{-1} km^{-1} towards the west. (b) Topography and χ index after stage 2, simulating the fault movement. (c) Histograms, mean values, and 1σ standard deviations for topographic metrics (χ index and mean upstream relief) at channel heads on the western and eastern flanks of the MDD, extracted from the modelled topography at the end of stage 2.

Data availability. All ^{10}Be data are available in Tables 2 and 3. Questions or request for DEM and shapefiles for topographic analysis can be sent to the corresponding author.

Author contributions. CHL and YBS conceptualized the study and conducted the field investigations with DEK and SMH. YBS was responsible for funding acquisition. CHL designed the ^{10}Be lab experiments with BYY. CHL and DEK performed all formal analysis and simulation. CHL, YBS, and JW prepared the manuscript with contributions from all co-authors.

Competing interests. The authors declare that they have no conflicts of interest.

Acknowledgements. We are grateful to Purevmaa Khandsuren for managing chemical treatment of ^{10}Be samples.

Financial support.

This research was supported by a grant (2022-MOIS62-001(RS-2022-ND640011)) of National Disaster Risk Analysis and Management Technology in Earthquake funded by Ministry of Interior and Safety (MOIS, Korea).

Reference

Attal, M., Cowie, P. A., Whittaker, A. C., Hobley, D., Tucker, G. E., and Roberts, G. P.: Testing fluvial erosion models using the transient response of bedrock rivers to tectonic forcing in the Apennines, Italy, J. Geophys. Res. Earth Surf., 116, https://doi.org/10.1029/2010JF001875, 2011.

Balco, G., Stone, J. O., Lifton, N. A., and Dunai, T. J.: A complete and easily accessible means of calculating surface exposure ages or erosion rates from 10Be and 26Al measurements, Quat. Geochronol., 3, 174–195, https://doi.org/10.1016/j.quageo.2007.12.001, 2008.

Barnhart, K. R., Hutton, E. W. H., Tucker, G. E., M. Gasparini, N., Istanbulluoglu, E., E. J. Hobley, D., J. Lyons, N., Mouchene, M., Siddhartha Nudurupati, S., M. Adams, J., and Bandaragoda, C.: Short communication: Landlab v2.0: A software package for Earth surface dynamics, Earth Surf. Dyn., 8, 379–397, https://doi.org/10.5194/esurf-8-379-2020, 2020.

Bierman, P. and Steig, E. J.: Estimating rates of denudation using cosmogenic isotope abundances in sediment, Earth Surf. Process. Landforms, 21, 125–139, https://doi.org/10.1002/(sici)1096-9837(199602)21:2<125::aid-esp511>3.0.co;2-8, 1996.

Bishop, P.: Drainage rearrangement by river capture, beheading and diversion, Prog. Phys. Geogr., 19, 449–473, https://doi.org/10.1177/030913339501900402, 1995.

von Blanckenburg, F.: The control mechanisms of erosion and weathering at basin scale from cosmogenic nuclides in river sediment, Earth Planet. Sci. Lett., 237, 462–479, https://doi.org/10.1016/j.epsl.2005.06.030, 2005.

Bonilla, M. G., Mark, R. K., and Lienkaemper, J. J.: Statistical relations among earthquake magnitude, surface rupture length, and surface fault displacement, Bull. Seismol. Soc. Am., 74, 2379–2411, 1984.

Bookhagen, B. and Burbank, D. W.: Topography, relief, and TRMM-derived rainfall variations along the Himalaya, Geophys. Res. Lett., 33, 1–5, https://doi.org/10.1029/2006GL026037, 2006.

Braucher, R., Merchel, S., Borgomano, J., and Bourlès, D. L.: Production of cosmogenic radionuclides at great depth: A multi element approach, Earth Planet. Sci. Lett., 309, 1–9, https://doi.org/10.1016/j.epsl.2011.06.036, 2011.

Braun, J. and Willett, S. D.: A very efficient O(n), implicit and parallel method to solve the stream power equation governing fluvial incision and landscape evolution, Geomorphology, 180–181, 170–179, https://doi.org/10.1016/j.geomorph.2012.10.008, 2013.

Brown, E. T., Stallard, R. F., Larsen, M. C., Raisbeck, G. M., and Yiou, F.: Denudation rates determined from the accumulation of in situ-produced 10Be in the luquillo experimental forest, Puerto Rico, Earth Planet. Sci. Lett., 129, 193–202, https://doi.org/10.1016/0012-821X(94)00249-X, 1995.

Bull, W. B.: Tectonic geomorphology of the Mojave Desert, California, 376 pp., 1977.

Bull, W. B. and McFadden, L. D.: Tectonic geomorphology north and south of the Garlock fault, California, in: Geomorphology in arid regions, Routledge, 115–138, 2020.

Burbank, D. W. and Anderson, R. S.: Tectonic geomorphology, John Wiley & Sons, 480 pp., 2011.

Campforts, B., Schwanghart, W., and Govers, G.: Accurate simulation of transient landscape evolution by eliminating numerical diffusion: The TTLEM 1.0 model, Earth Surf. Dyn., 5, 47–66, https://doi.org/10.5194/esurf-5-47-2017, 2017.

Cartwright, J. A., Trudgill, B. D., and Mansfield, C. S.: Fault growth by segment linkage: an explanation for scatter in maximum displacement and trace length data from the Canyonlands Grabens of SE Utah, J. Struct. Geol., 17, 1319–1326, https://doi.org/10.1016/0191-8141(95)00033-A, 1995.

Charreau, J., Blard, P. H., Zumaque, J., Martin, L. C. P., Delobel, T., and Szafran, L.: Basinga: A cell-by-cell GIS toolbox for computing basin average scaling factors, cosmogenic production rates and denudation rates, Earth Surf. Process. Landforms, 44, 2349–2365, https://doi.org/10.1002/esp.4649, 2019.

Cheon, Y., Son, M., Song, C. W., Kim, J. S., and Sohn, Y. K.: Geometry and kinematics of the Ocheon Fault System along the boundary between the Miocene Pohang and Janggi basins, SE Korea, and its tectonic implications, Geosci. J., 16, 253–273, https://doi.org/10.1007/s12303-012-0029-0, 2012.

Cheon, Y., Choi, J. H., Kim, N., Lee, H., Choi, I., Bae, H., Rockwell, T. K., Lee, S. R., Ryoo, C. R., Choi, H., and Lee, T. H.: Late Quaternary transpressional earthquakes on a long-lived intraplate fault: A case study of the Southern Yangsan Fault, SE Korea, Quat. Int., 553, 132–143, https://doi.org/10.1016/j.quaint.2020.07.025, 2020a.

Cheon, Y., Ha, S., Lee, S., and Son, M.: Tectonic evolution of the Cretaceous Gyeongsang Back-arc Basin, SE Korea: Transition from sinistral transtension to strike-slip kinematics, Gondwana Res., 83, 16–35, https://doi.org/10.1016/j.gr.2020.01.012, 2020b.

Cheon, Y., Shin, Y. H., Park, S., Choi, J. H., Kim, D. E., Ko, K., Ryoo, C. R., Kim, Y. S., and Son, M.: Structural architecture and late Cenozoic tectonic evolution of the Ulsan Fault Zone, SE Korea: New insights from integration of geological and geophysical data, Front. Earth Sci., 11, 1–14, https://doi.org/10.3389/feart.2023.1183329, 2023.

Cheong, C. S., Hong, D. G., Lee, K. S., Kim, J. W., Choi, J. H., Murray, A. S., Chwae, U., Im, C. B., Chang, C. J., and Chang, H. W.: Determination of slip rate by optical dating of fluvial deposits from the Wangsan fault, SE Korea, Quat. Sci. Rev., 22, 1207–1211, https://doi.org/10.1016/S0277-3791(03)00020-9, 2003.

Chmeleff, J., von Blanckenburg, F., Kossert, K., and Jakob, D.: Determination of the 10Be half-life by multicollector ICP-MS and liquid scintillation counting, Nucl. Instruments Methods Phys. Res. Sect. B Beam Interact. with Mater. Atoms, 268, 192–199, https://doi.org/10.1016/j.nimb.2009.09.012, 2010.

Choi, J. H., Murray, A. S., Jain, M., Cheong, C. S., and Chang, H. W.: Luminescence dating of well-sorted marine terrace sediments on the southeastern coast of Korea, Quat. Sci. Rev., 22, 407–421, https://doi.org/10.1016/S0277-3791(02)00136-1, 2003a.

Choi, J. H., Murray, A. S., Cheong, C. S., Hong, D. G., and Chang, H. W.: The resolution of stratigraphic inconsistency in the luminescence ages of marine terrace sediments from Korea, Quat. Sci. Rev., 22, 1201–1206, https://doi.org/10.1016/S0277-3791(03)00022-2, 2003b.

Choi, J. H., Kim, J. W., Murray, A. S., Hong, D. G., Chang, H. W., and Cheong, C. S.: OSL dating of marine terrace sediments on the southeastern coast of Korea with implications for Quaternary tectonics, Quat. Int., 199, 3–14, https://doi.org/10.1016/j.quaint.2008.07.009, 2009.

Choi, K. H., Seong, Y. B., Jung, P. M., and Lee, S. Y.: Using cosmogenic 10Be dating to unravel the antiquity of a rocky shore platform on the West Coast of Korea, J. Coast. Res., 28, 641–657, https://doi.org/10.2112/JCOASTRES-D-11-00087.1, 2012a.

Choi, S.-J., Jun, J. S., Song, K.-Y., Kim, H., Kihm, Y. H., Choi, P., Chwae, U., Han, J.-G., Ryoo, C.-R., Sun, C.-G., Jun, M.-S., Kim, G.-Y., Kim, Y. B., Lee, H. J., Shin, J. S., Lee, Y. S., and Kee, W.-S.: Active Fault Map and Seismic Hazard Map, Seoul, 939 pp., 2012b.

Choi, S. J., Merritts, D. J., and Ota, Y.: Elevations and ages of marine terraces and late Quaternary rock uplift in southeastern Korea, J. Geophys. Res. Solid Earth, 113, 1–15, https://doi.org/10.1029/2007JB005260, 2008.

Choi, S. J., Jeon, J. S., Choi, J. H., Kim, B., Ryoo, C. R., Hong, D. G., and Chwae, U.: Estimation of possible maximum earthquake magnitudes of Quaternary faults in the southern Korean Peninsula, Quat. Int., 344, 53–63, https://doi.org/10.1016/j.quaint.2014.05.052, 2014.

Choi, W. H.: Neotectonics of the Gyeongju-Ulsan area in the southeastern part of Korean Peninsula, Seoul National University, 2005 pp., 2003.

Choi, W. H., Chang, C. joong, and Inoue, D.: Fault segmentation along the Ulsan Fault System based on criteria of segment type, 78–85, 2006.

Cox, R. T.: Analysis of drainage-basin symmetry as a rapid technique to identify areas of possible Quaternary tilt-block tectonics: an example from the Mississippi Embayment, Geol. Soc. Am. Bull., 106, 571–581, https://doi.org/10.1130/0016-7606(1994)106<0571:AODBSA>2.3.CO;2, 1994.

Crosby, B. T. and Whipple, K. X.: Knickpoint initiation and distribution within fluvial networks: 236 waterfalls in the Waipaoa River, North Island, New Zealand, Geomorphology, 82, 16–38, https://doi.org/10.1016/j.geomorph.2005.08.023, 2006.

Culling, W. E. H.: Soil Creep and the Development of Hillside Slopes, J. Geol., 71, 127–161, https://doi.org/10.1086/626891, 1963.

Cyr, A. J., Granger, D. E., Olivetti, V., and Molin, P.: Quantifying rock uplift rates using channel steepness and cosmogenic nuclide-determined erosion rates: Examples from northern and southern Italy, Lithosphere, 2, 188–198, https://doi.org/10.1130/L96.1, 2010.

Cyr, A. J., Granger, D. E., Olivetti, V., and Molin, P.: Distinguishing between tectonic and lithologic controls on bedrock channel longitudinal profiles using cosmogenic 10Be erosion rates and channel steepness index, Geomorphology, 209, 27–38, https://doi.org/10.1016/j.geomorph.2013.12.010, 2014.

Dawers, H.: Displacement-length scaling and fault linkage, J. Struct. Geol., 17, 607–614, 1995.

DiBiase, R. A., Whipple, K. X., Heimsath, A. M., and Ouimet, W. B.: Landscape form and millennial erosion rates in the San Gabriel Mountains, CA, Earth Planet. Sci. Lett., 289, 134–144, https://doi.org/10.1016/j.epsl.2009.10.036, 2010.

Duvall, A., Kirby, E., and Burbank, D.: Tectonic and lithologic controls on bedrock channel profiles and processes in coastal California, J. Geophys. Res. Earth Surf., 109, 1–18, https://doi.org/10.1029/2003jf000086, 2004.

Fernandes, F. and Dietrich, E.: Hillslope evolution by diffusive processes: The timescale for equilibrium adjustments, Water Resour. Res., 33, 1307–1318, 1997.

Flint, J. J.: Stream gradient as a function of order, magnitude, and discharge, Water Resour. Res., 10, 969–973, https://doi.org/10.1029/WR010i005p00969, 1974.

Forte, A. M. and Whipple, K. X.: Criteria and tools for determining drainage divide stability, Earth Planet. Sci. Lett., 493, 102–117, https://doi.org/10.1016/j.epsl.2018.04.026, 2018.

Gilbert, G. K.: Geology of the Henry Mountains, Washington, D.C., 160 pp., https://doi.org/10.3133/70038096, 1877.

Goren, L., Willett, S. D., Herman, F., and Braun, J.: Coupled numerical-analytical approach to landscape evolution modeling, Earth Surf. Process. Landforms, 39, 522–545, https://doi.org/10.1002/esp.3514, 2014.

Granger, D. E., Kirchner, J. W., and Finkel, R.: Spatially averaged long-term erosion rates measured from in situ-produced cosmogenic nuclides in alluvial sediment, J. Geol., 104, 249–257, https://doi.org/10.1086/629823, 1996.

Hack, J. T.: Stream-profile analysis and stream-gradient index, J. Res. US Geol. Surv., 1, 421–429, 1973.

Han, J. W.: Uplift history of the Taebaeksan Range in the Daegwallyeong area using fission track analysis, Seoul National University, 107 pp., 2002.

Han, M., Kim, K. H., Son, M., and Kang, S. Y.: Current microseismicity and generating faults in the Gyeongju area, southeastern Korea, Tectonophysics, 694, 414–423, https://doi.org/10.1016/j.tecto.2016.11.026, 2017.

Harel, M. A., Mudd, S. M., and Attal, M.: Global analysis of the stream power law parameters based on worldwide 10Be denudation rates, Geomorphology, 268, 184–196, https://doi.org/10.1016/j.geomorph.2016.05.035, 2016.

He, C., Yang, C. J., Turowski, J. M., Rao, G., Roda-Boluda, D. C., and Yuan, X. P.: Constraining tectonic uplift and advection from the main drainage divide of a mountain belt, Nat. Commun., 12, https://doi.org/10.1038/s41467-020-20748-2, 2021.

Heo, S., Choi, J.-H., and Hong, D.-G.: Revisiting the OSL Ages of Marine Terrace Sediments at Suryum Fault Site, Gyeongju, South Korea: Single Grain OSL Dating, J. Petrol. Soc. Korea, 23, 187–195, https://doi.org/10.7854/jpsk.2014.23.3.187, 2014.

Hobley, D. E. J., Adams, J. M., Siddhartha Nudurupati, S., Hutton, E. W. H., Gasparini, N. M., Istanbulluoglu, E., and Tucker, G. E.: Creative computing with Landlab: An open-source toolkit for building, coupling, and exploring two-dimensional numerical models of Earth-surface dynamics, Earth Surf. Dyn., 5, 21–46, https://doi.org/10.5194/esurf-5-21-2017, 2017.

Hoskins, A. M., Attal, M., Mudd, S. M., and Castillo, M.: Topographic Response to Horizontal Advection in Normal Fault-Bound Mountain Ranges, J. Geophys. Res. Earth Surf., 128, 1–30, https://doi.org/10.1029/2023JF007126, 2023.

Howard, A. D. and Kerby, G.: Channel changes in badlands, Geol. Soc. Am. Bull., 94, 739–752, https://doi.org/10.1130/0016-7606(1983)94<739:CCIB>2.0.CO;2, 1983.

Hu, K., Fang, X., Ferrier, K. L., Granger, D. E., Zhao, Z., and Ruetenik, G. A.: Covariation of cross-divide differences in denudation rate and χ: Implications for drainage basin reorganization in the Qilian Shan, northeast Tibet, Earth Planet. Sci. Lett., 562, 116812, https://doi.org/10.1016/j.epsl.2021.116812, 2021.

Hutton, E., Barnhart, K., Hobley, D., Tucker, G., Nudurupati, S. S., Adams, J., Gasparini, N. M., Shobe, C., Strauch, R., Knuth, J., margauxmouchene, Lyons, N., DavidLitwin, Glade, R., Giuseppecipolla95, Manaster, A., alangston, Thyng, K., and Rengers, F.: landlab/landlab: Mrs. Weasley, https://doi.org/10.5281/zenodo.3776837, 2020.

Jeong, A., Seong, Y. B., Lee, C. H., and Choi, K. H.: A numerical model study for simulation of rocky coast evolution and erosion using cosmogenic nuclides: A case study along the Dunduri and Dokdo shore platform in Korea, J. Geol. Soc. Korea, 57, 195–207, https://doi.org/10.14770/jgsk.2021.57.2.195, 2021.

Kang, P.-C.: Geological analysis of Landsat imagery of South Korea (I), J. Geol. Soc. Korea, 15, 109–126, 1979a.

Kang, P.-C.: Geological analysis of Landsat imagery of South Korea (II), J. Geol. Soc. Korea, 15, 181–191, 1979b.

Kee, W.-S., Kim, S. W., Kim, H., Hong, P., Kwon, C. W., Lee, H.-J., Cho, D.-L., Koh, H. J., Song, K.-Y., Byun, U.-H., Jang, Y., and Lee, B. C.: Geologic Map of Korea (1:1,000,000), Daejeon, https://doi.org/10.22747/data.20220816.4826, 2019.

Keller, E. A. and Pinter, N.: Active tectonics, Prentice Hall Upper Saddle River, NJ, 338 pp., 1996.

Kim, D. E., Seong, Y. B., Byun, J., Weber, J., and Min, K.: Geomorphic disequilibrium in the Eastern Korean Peninsula: Possible evidence for reactivation of a rift-flank margin, Geomorphology, 254, 130–145, https://doi.org/10.1016/j.geomorph.2015.11.022, 2016a.

Kim, D. E., Seong, Y. B., Weber, J., and Yu, B. Y.: Unsteady migration of Taebaek Mountain drainage divide, Cenozoic extensional basin margin, Korean Peninsula, Geomorphology, 352, https://doi.org/10.1016/j.geomorph.2019.107012, 2020.

Kim, J. H., Kang, P. C., and Lim, J. U.: A Study of the Relation between Geologic Structures and Ore Deposits in Ryeongna Province using Landsat-1 Images, J. Geol. Soc. Korea, 12, 79–89, 1976.

Kim, J. W., Chang, H. W., Choi, J. H., Choi, K. hee, and Byun, J. M.: Landform Characteristics of Coastal Terraces and Optically Stimulated Luminescence Dating on the Terrace Deposits in Yangnam and Yangbuk Area of the Gyeongju City, South Korea, J. Korean Geomorphol. Assoc., 14, 1–14, 2007.

Kim, M.-C., Jung, S., Yoon, S., Jeong, R.-Y., Song, C. W., and Son, M.: Neotectonic Crustal Deformation and Current Stress Field in the Korean Peninsula and Their Tectonic Implications: A Review, J. Petrol. Soc. Korea, 25, 169–193, https://doi.org/10.7854/jpsk.2016.25.3.169, 2016b.

Kim, N., Park, S. I., Cho, C. S., Cheon, Y., and Peace, A. L.: Neotectonic transpressional intraplate deformation in eastern Eurasia: Insights from active fault systems in the southeastern Korean Peninsula, Geosci. Front., 14, 101559, https://doi.org/10.1016/j.gsf.2023.101559, 2023a.

Kim, S. W.: A Study on the Terraces Along the Southern Coast (Bang-eojin-Pohang) of the Korean Peninsula, J. Geol. Soc. Korea, 9, 89–121, 1973.

Kim, T., Kim, D., Kim, S., Seong, Y. B., Lim, H. S., Shin, H., and Kim, Y.: Kinematic characteristics and movement timing of the Wonwonsa fault in the central Ulsan Fault, J. Geol. Soc. Korea, 57, 35–48, 2021.

Kim, T., Choi, J. H., Cheon, Y., Lee, T. H., Kim, N., Lee, H., Kim, C. M., Choi, Y., Bae, H., Kim, Y. S., Ryoo, C. R., and Klinger, Y.: Correlation of paleoearthquake records at multiple sites along the southern Yangsan Fault, Korea: Insights into rupture scenarios of intraplate strike-slip earthquakes, Tectonophysics, 854, 229817, https://doi.org/10.1016/j.tecto.2023.229817, 2023b.

Kirby, E. and Whipple, K.: Quantifying differential rock-uplift rates via stream profile analysis, Geology, 29, 415–418, https://doi.org/10.1130/0091-7613(2001)029<0415:QDRURV>2.0.CO;2, 2001.

Kirby, E. and Whipple, K. X.: Expression of active tectonics in erosional landscapes, J. Struct. Geol., 44, 54–75, https://doi.org/10.1016/j.jsg.2012.07.009, 2012.

Kohl, C. P. and Nishiizumi, K.: Chemical isolation of quartz for measurement of in-situ -produced cosmogenic nuclides, Geochim. Cosmochim. Acta, 56, 3583–3587, https://doi.org/10.1016/0016-7037(92)90401-4, 1992.

Kyung, J. B.: Paleoseismological study on the mid-northern part of Ulsan Fault by trench method, 1997.

Kyung, J. B.: Paleoseismological study and evaluation of maximum earthquake magnitude along the Yangsan and Ulsan Fault Zones in the southeastern part of Korea, Geophys. Geophys. Explor., 13, 187–197, 2010.

Lal, D.: Cosmic ray labeling of erosion surfaces: in situ nuclide production rates and erosion models, Earth Planet. Sci. Lett., 104, 424–439, https://doi.org/10.1016/0012-821X(91)90220-C, 1991.

Lee, C. H., Seong, Y. B., Schoenbohm, L. M., Kim, D. E., and Yu, B. Y.: Geomorphic constraints on the development of a blind-thrust induced landform, south-central Mongolia: Insights into foreberg growth, Geomorphology, 378, 107613, https://doi.org/10.1016/j.geomorph.2021.107613, 2021.

Lee, S. Y., Seong, Y. B., Kang, H. C., Choi, K. H., and Yu, B. Y.: Cosmogenic10Be and OSL dating of marine terraces along the central-east coast of korea: Spatio-temporal variations in uplift rates, Open Geogr. J., 7, 28–39, https://doi.org/10.2174/1874923201507010028, 2015.

Lifton, N., Sato, T., and Dunai, T. J.: Scaling in situ cosmogenic nuclide production rates using analytical approximations to atmospheric cosmic-ray fluxes, Earth Planet. Sci. Lett., 386, 149–160, https://doi.org/10.1016/j.epsl.2013.10.052, 2014.

Manighetti, I., Caulet, C., De Barros, L., Perrin, C., Cappa, F., and Gaudemer, Y.: Generic along-strike segmentation of Afar normal faults, East Africa: Implications on fault growth and stress heterogeneity on seismogenic fault planes, Geochemistry, Geophys. Geosystems, 16, 443–467, https://doi.org/10.1002/2014GC005691.Received, 2015.

Marliyani, G. I., Arrowsmith, J. R., and Whipple, K. X.: Characterization of slow slip rate faults in humid areas: Cimandiri fault zone, Indonesia, J. Geophys. Res. Earth Surf., 121, 2287–2308, https://doi.org/10.1002/2016JF003846, 2016.

McCalpin, J. P.: Application of paleoseismic data to seismic hazard assessment and neotectonic research, in: International Geophysics, vol. 62, Elsevier, 439–493, 1996.

Min, K., Cho, M., and Reiners, P. W.: Coeval exhumation of Korean Peninsula and opening of East Sea revealed from single-grain (U-Th)/He thermochronology, in: 12th International Conference on Thermochronology, 265, 2010.

Moore, J. M. and Schultz, R. A.: Processes of faulting in jointed rocks of Canyonlands National Park, Utah, Bull. Geol. Soc. Am., 111, 808–822, https://doi.org/10.1130/0016-7606(1999)111<0808:POFIJR>2.3.CO;2, 1999.

Moss, R. E. S. and Ross, Z. E.: Probabilistic fault displacement hazard analysis for reverse faults, Bull. Seismol. Soc. Am., 101, 1542–1553, https://doi.org/10.1785/0120100248, 2011.

Mudd, S. M., Attal, M., Milodowski, D. T., Grieve, S. W. D., and Valters, D. A.: A statistical framework to quantify spatial variation in channel gradients using the integral method of channel profile analysis, J. Geophys. Res. Earth Surf., 119, 138–152, https://doi.org/10.1002/2013JF002981, 2014.

Muscheler, R., Beer, J., Kubik, P. W., and Synal, H. A.: Geomagnetic field intensity during the last 60,000 years based on 10Be and 36Cl from the Summit ice cores and 14C, Quat. Sci. Rev., 24, 1849–1860, https://doi.org/10.1016/j.quascirev.2005.01.012, 2005.

Naik, S. P., Gwon, O., Park, K., Bae, S. Y., Shin, H. C., Choi, J. H., and Kim, Y. S.: Localization and characterization of the southern Ulsan fault (UF) using geo-electrical imaging: Implication for seismic hazard assessment in an urbanized area, J. Geodyn., 151, 101919, https://doi.org/10.1016/j.jog.2022.101919, 2022.

Nishiizumi, K., Imamura, M., Caffee, M. W., Southon, J. R., Finkel, R. C., and McAninch, J.: Absolute calibration of 10Be AMS standards, Nucl. Instruments Methods Phys. Res. Sect. B Beam Interact. with Mater. Atoms, 258, 403–413, https://doi.org/10.1016/j.nimb.2007.01.297, 2007.

Okada, A., Watanabe, M., Suzuki, Y., Kyung, J.-B., Jo, W.-R., Kim, S.-K., Oike, K., and Nakamura, T.: Active Fault Topography and Fault Outcrops in the Central Part of the Ulsan Fault System, Southeast Korea, J. Geogr. (Chigaku Zasshi), 107, 644–658, https://doi.org/10.5026/jgeography.107.5_644, 1998.

Okada, A., Takemura, K., Watanabe, M., Suzuki, Y., and Kyung, J.-B.: Trench excavation surveys across the Yangsan and Ulsan active fault systems in the southeastern part of Korean peninsula, Japanese Geomorphol. Union, 22, 287–306, 2001.

Park, Y., Ree, J. H., and Yoo, S. H.: Fault slip analysis of Quaternary faults in southeastern Korea, Gondwana Res., 9, 118–125, https://doi.org/10.1016/j.gr.2005.06.007, 2006.

Perron, J. T. and Royden, L.: An integral approach to bedrock river profile analysis, Earth Surf. Process. Landforms, 38, 570–576, https://doi.org/10.1002/esp.3302, 2013.

Portenga, E. W., Bierman, P. R., Duncan, C., Corbett, L. B., Kehrwald, N. M., and Rood, D. H.: Erosion rates of the Bhutanese Himalaya determined using in situ-produced 10Be, Geomorphology, 233, 112–126, https://doi.org/10.1016/j.geomorph.2014.09.027, 2015.

Reitman, N. G., Mueller, K. J., Tucker, G. E., Gold, R. D., Briggs, R. W., and Barnhart, K. R.: Offset Channels May Not Accurately Record Strike-Slip Fault Displacement: Evidence From Landscape Evolution Models, J. Geophys. Res. Solid Earth, 124, 13427–13451, https://doi.org/10.1029/2019JB018596, 2019.

Royden, L. and Perron, J. T.: Solutions of the stream power equation and application to the evolution of river longitudinal profiles, J. Geophys. Res. Earth Surf., 118, 497–518, https://doi.org/10.1002/jgrf.20031, 2013.

Ryang, W. H., Simms, A. R., Yoon, H. H., Chun, S. S., and Kong, G. S.: Last interglacial sea-level proxies in the Korean Peninsula, Earth Syst. Sci. Data, 14, 117–142, https://doi.org/10.5194/essd-14-117-2022, 2022.

Ryoo, C.-R., Lee, B. J., Son, M., Lee, Y. H., Choi, S.-J., and Chwae, U.: Quaternary faults in Gaegok-ri, Oedong-eup, Gyeongju, Korea, J. Geol. Soc. Korea, 38, 309–323, 2002.

Ryoo, C.: A Report for the Quaternary Gaegok 6 Fault Developed in the Mid-eastern Part of Ulsan Fault Zone , Korea, Econ. Environ. Geol., 42, 635–643, 2009.

Scherler, D., Bookhagen, B., and Strecker, M. R.: Tectonic control on 10Be-derived erosion rates in the Garhwal Himalaya, India, J. Geophys. Res. Earth Surf., 119, 83–105, https://doi.org/10.1002/2013JF002955, 2014.

Schwanghart, W. and Scherler, D.: Short Communication: TopoToolbox 2 - MATLAB-based software for topographic analysis and modeling in Earth surface sciences, Earth Surf. Dyn., 2, 1–7, https://doi.org/10.5194/esurf-2-1-2014, 2014.

Seidl, M. A. and Dietrich, W. E.: The problem of channel erosion into bedrock, Catena Suppl., 23, 101–124, 1992.

Seong, Y. B., Dorn, R. I., and Yu, B. Y.: Evaluating the life expectancy of a desert pavement, Earth-Science Rev., 162, 129–154, https://doi.org/10.1016/j.earscirev.2016.08.005, 2016.

Sklar, L., Dietrich, E., and Kppfgka, K.: Profiles and Bedrock Incision Models : Stream Power and the Influence of Sediment Supply, Rivers over rock Fluv. Process. bedrock channels, Geophys. Monogr. Ser., 237–260, 1998.

Slemmons, D. B. and Depolo, C. M.: Evaluation of active faulting and associated hazards, in: Active Tectonics, National Academy Press Washington, DC, 45–62, 1986.

Snyder, N. P., Whipple, K. X., Tucker, G. E., and Merritts, D. J.: Stream profiles in the Mendocino triple junction region, northern California, GSA Bull., 112, 1250–1263, 2000.

Son, M., Song, C. W., Kim, M. C., Cheon, Y., Cho, H., and Sohn, Y. K.: Miocene tectonic evolution of the basins and fault systems, SE Korea: Dextral, simple shear during the East Sea (Sea of Japan) opening, J. Geol. Soc. London., 172, 664–680, https://doi.org/10.1144/jgs2014-079, 2015.

Stephenson, S. N., Roberts, G. G., Hoggard, M. J., and Whittaker, A. C.: A Cenozoic uplift history of Mexico and its surroundings from longitudinal river profiles, Geochemistry, Geophys. Geosystems, 15, 4734–4758, https://doi.org/10.1002/2014GC005425.Received, 2014.

Stock, J. D. and Montgomery, D. R.: Geologic constraints on bedrock river incision using the stream power law, J. Geophys. Res. Solid Earth, 104, 4983–4993, https://doi.org/10.1029/98jb02139, 1999.

Stone, J. O.: Air pressure and cosmogenic isotope production, J. Geophys. Res., 105, 23753–23759, 2000.

Strahler, A. N.: Hypsometric (area-altitude) analysis of erosional topography, Bull. Geol. Soc. Am., 63, 1117–1142, 1952.

Su, Q., Wang, X., Lu, H., and Xie, H.: Dynamic divide migration as a response to asymmetric uplift: An example from the Zhongtiao Shan, North China, Remote Sens., 12, 1–14, https://doi.org/10.3390/rs12244188, 2020.

Taylor, M., Forte, A., Laskowski, A., and Ding, L.: Active uplift of southern tibet revealed, GSA Today, 31, https://doi.org/10.1130/GSATG487A.1, 2021.

Temme, A. J. A. M., Armitage, J., Attal, M., van Gorp, W., Coulthard, T. J., and Schoorl, J. M.: Developing, choosing and using landscape evolution models to inform field-based landscape reconstruction studies, Earth Surf. Process. Landforms, 42, 2167–2183, https://doi.org/10.1002/esp.4162, 2017.

Tucker, G. E. and Bras, R. L.: Hillslope processes, drainage density, and landscape morphology, Water Resour., 34, 2751–2764, 1998.

Tucker, G. E. and Whipple, K. X.: Topographic outcomes predicted by stream erosion models: Sensitivity analysis and intermodel comparison, J. Geophys. Res. Solid Earth, 107, 1–16, https://doi.org/10.1029/2001jb000162, 2002.

Tucker, G. E., Lancaster, S. T., Gasparini, N. M., and Bras, R. L.: The channel-hillslope integrated landscape development model, in: Landscape Erosion and Evolution Modeling, 349–388, https://doi.org/10.1007/978-1-4615-0575-4, 2001.

Wells, D. L. and Coppersmith, K. J.: New empirical relationships among magnitude, rupture length, rupture width, rupture area, and surface displacement, Bull. - Seismol. Soc. Am., 84, 974–1002, https://doi.org/10.1785/bssa0840040974, 1994.

Whipple, K. X. and Tucker, G. E.: Dynamics of the stream-power river incison model: Implications for height limits of mountain ranges, landscape response timescales, and research needs, J. Geophys. Res., 104, 17661–17674, 1999.

Whipple, K. X. and Tucker, G. E.: Implications of sediment-flux-dependent river incision models for landscape evolution, J. Geophys. Res. Solid Earth, 107, https://doi.org/10.1029/2000jb000044, 2002.

Whipple, K. X., Forte, A. M., DiBiase, R. A., Gasparini, N. M., and Ouimet, W. B.: Timescales of landscape response to divide migration and drainage capture: Implications for the role of divide mobility in landscape evolution, J. Geophys. Res. Earth Surf., 122, 248–273, https://doi.org/10.1002/2016JF003973, 2017.

Willett, S. D., McCoy, S. W., Taylor Perron, J., Goren, L., and Chen, C. Y.: Dynamic reorganization of River Basins, Science (80-.)., 343, https://doi.org/10.1126/science.1248765, 2014.

Wobus, C., Whipple, K. X., Kirby, E., Snyder, N., Johnson, J., Spyropolou, K., Crosby, B., and Sheehan, D.: Tectonics from topography: Procedures, promise, and pitfalls, Spec. Pap. Geol. Soc. Am., 398, 55–74, https://doi.org/10.1130/2006.2398(04), 2006.

Zebari, M., Grützner, C., Navabpour, P., and Ustaszewski, K.: Relative timing of uplift along the Zagros Mountain Front Flexure (Kurdistan Region of Iraq): Constrained by geomorphic indices and landscape evolution modeling, Solid Earth, 10, 663–682, https://doi.org/10.5194/se-10-663-2019, 2019.

Zeng, X. and Tan, X.: Drainage divide migration in response to strike-slip faulting: An example from northern Longmen Shan, eastern Tibet, Tectonophysics, 848, 229720, https://doi.org/10.1016/j.tecto.2023.229720, 2023.

Zhou, C. and Tan, X.: Quantifying the influence of asymmetric uplift, base level elevation, and erodibility on cross-divide χ difference, Geomorphology, 427, https://doi.org/10.1016/j.geomorph.2023.108634, 2023.

Zhou, C., Tan, X., Liu, Y., Lu, R., Murphy, M. A., He, H., Han, Z., and Xu, X.: Ongoing westward migration of drainage divides in eastern Tibet, quantified from topographic analysis, Geomorphology, 402, 108123, https://doi.org/10.1016/j.geomorph.2022.108123, 2022.